Riverine organic matter dynamics in the headwater of the Yellow River under climate change

Xiaoxiao Wang [1,2], Jie Wang [1], Tianqing Ren [1], Jun Zhou [3]

[1] School of Geographical Sciences, China West Normal University, Nanchong 637009, China

[2] Sichuan Provincial Engineering Research Center of Monitoring and Control for Soil Erosion in Dry Valleys, China West Normal University, Nanchong 637009, China

[3] Institute of Mountain Hazards and Environment, Chinese Academy of Sciences, Chengdu 610213, China

Correspondence to: Xiaoxiao Wang (wxx1989@cwnu.edu.cn)

Xiaoxiao Wang and Jie Wang contributed equally to this work.

Abstract： Alpine headwater streams play a crucial role in the global carbon cycle and are particularly sensitive to climate change. Riverine organic matter (ROM) mediates the transport and transformation of terrestrial carbon across aquatic systems. However, how ROM responds to climate change in the headwaters of the Qinghai-Tibetan Plateau (QTP) remains poorly understood, largely owing to a lack of long-term, high-spatial-resolution in-situ measurements. In this study, we used machine learning models combining satellite data and geographical variables to reconstruct historical variations in Chemical Oxygen Demand (COD_{Mn}, a proxy for ROM) along the Yellow River's Headstream (YRHS), and to predict future changes under typical Shared Socioeconomic Pathways. The results indicate that COD_{Mn} levels in the midstream region of the YRHS, characterized by greater precipitation, higher soil organic matter, and denser vegetation, were relatively high (2.73 ± 1.63 mg L^{-1}) and exhibited an increasing trend (0.575 mg L^{-1}) over the past decade. Driven primarily by increasing precipitation and temperature, COD_{Mn} levels are projected to rise in upstream and downstream areas but decline at midstream sites under SSP126, SSP245, and SSP585 by 2100. The annual export of riverine organic matter from the midstream of the YRHS is expected to remain stable by 2100. Therefore, our findings identify the midstream region of the YRHS as a critical and climate-sensitive region for organic matter dynamics. Though our study provides a comprehensive understanding of how climate change is reshaping riverine organic matter dynamics, substantial uncertainties remain in the future riverine organic matter changes owing to the complex interactions among precipitation, warming, hydrology and their combined effects on carbon cycles in alpine catchments.

Key words: Alpine River; Carbon cycle; Climate change; Remote sensing; Qinghai–Tibetan Plateau

1 Introduction

Alpine regions represent some of the most vulnerable ecosystems to climate change, experiencing temperature increases nearly twice the global average (Kotlarski et al., 2023; Aryal and Pokhrel, 2025). Among them, the Qinghai–Tibetan Plateau (QTP), often referred to as the “Third Pole”, is the highest and one of the most climate-sensitive regions on Earth (Chen et al., 2022; Wang et al., 2023). In recent decades, the accelerated warming has triggered widespread environmental changes on the QTP, which are expected to significantly alter the sources, forms, and fluxes of carbon exports associated with permafrost degradation (Chen et al., 2022; Xu et al., 2024; Hong et al., 2025). Studies have shown that parts of the QTP have already shifted from carbon sinks to carbon sources and lateral transport of carbon has increased the riverine carbon fluxes on the QTP (L. Li et al., 2025). Riverine organic matter (ROM) plays a pivotal role in the biogeochemical cycles of carbon (Hu et al., 2020; Giri, 2021; Regnier et al., 2022; Beusen et al., 2022), and the increase in ROM will pose threats to the water quality of rivers on the QTP. Despite growing concern regarding the ROM and its ecological consequences, our understanding of ROM dynamics across the QTP remains limited. Therefore, there is an urgent need for high spatial resolution and long-term observations of ROM dynamics and their exports on the QTP.

Headwater streams account for approximately 61% of total riverine carbon efflux despite representing only 34–38% of total stream surface area (Li et al., 2021). Over recent decades, climate change has substantially influenced the carbon dynamics of headstreams on the QTP (Yao et al., 2022; L. Li et al., 2025). Long-term records show that the annual streamflow of headstreams in this region has generally increased over the past six decades (1962–2019) (Zhang et al., 2024). Warming and wetting trends have contributed to higher ROM in the headwaters (Xu et al., 2024).

Furthermore, climate-induced changes have intensified sediment erosion and enhanced associated ROM transport processes across the QTP (Zhao et al., 2023; Li et al., 2024; J. Li et al., 2025). Nevertheless, fewer than 30% of headstreams across the QTP are consistently monitored (Li et al., 2024), leaving the responses of ROM dynamics in headwaters to climate change poorly constrained.

The limited understanding of ROM dynamics in alpine headwaters is largely due to the scarcity of long-term, continuous in-situ measurements, where data collection remains logistically challenging. In recent years, advances in remote sensing and machine learning have provided powerful alternatives for addressing these limitations, offering new opportunities to predict water quality and infer nutrient-related parameters across extensive spatial and temporal scales (Adegun et al., 2023; Zeng et al., 2023; Zhi et al., 2024). Satellite-derived indices such as reflectance ratios, the Normalized Difference Chlorophyll Index (NDCI), the Suspended Sediment Index (SSI), etc., have been increasingly employed to assess riverine organic matter, particularly when integrated with machine learning algorithms (Liu et al., 2021; Deng et al., 2024; Yan et al., 2025). Consequently, integrating remote sensing data with in-situ measurements and machine learning holds significant potential for improving our understanding of ROM in headwaters and their responses to ongoing climate change.

The Yellow River's headstream (YRHS), located on the eastern QTP, constitute a crucial component of QTP's water resources and carbon cycling systems and have undergone substantial environmental changes in recent decades (Wen et al., 2024). Current study indicated that approximately 35% of the Yellow River's source region serves as a net carbon source, and the lateral transport of carbon accounts for 31% of net ecosystem production in the Yellow River's

source region (L. Li et al., 2025). The YRHS lies in a transition zone between permafrost and seasonally frozen ground, where climate warming has driven substantial permafrost degradation and triggered a cascade of environmental and ecological issues (Yang et al., 2023). While riverine organic matter dynamics have been extensively studied across the Yellow River Basin (Deng et al., 2025; Lan et al., 2025), the long-term and projected trajectories of ROM in its headwater region have received little attention, which is largely attributable to limited monitoring network coverage in this region. Therefore, given the critical role of the Yellow River headwaters in carbon cycling and downstream water quality and its sensitivity to climate change, there is an urgent need to investigate the dynamics of riverine organic matter in the headwaters of the Yellow River under climate change.

According to previous studies, ROM was estimated using the permanganate index (COD_{Mn}) as a proxy across China (Jiao et al., 2021; Lv et al., 2024; X. Wang et al., 2025; Shang et al., 2026), and significant linear relationships exist between COD_{Mn} and dissolved organic carbon across various aquatic environments (Shang et al., 2026; Wang et al., 2026). Therefore, COD_{Mn} can be used as a proxy for riverine organic matter in the alpine study area. Accordingly, in this study, we focus on the source region of the Yellow River to develop COD_{Mn} predictive models by combining in situ water quality observations with satellite reflectance data and to assess future changes under the SSP126, SSP245, and SSP585 scenarios. The objectives are to: (1) quantify the decadal variability of COD_{Mn} in the headstreams of the Yellow River and identify its driving factors; (2) predict future changes in COD_{Mn} under projected climate change scenarios; and (3) estimate COD_{Mn} exports and assess their potential impacts on downstream ecosystems. This study aims to provide a comprehensive and scalable understanding of how climate change is reshaping riverine

101 organic matter dynamics within one of the world's most critical headwater regions.

102 **2 Methods and materials**

103 **2.1 Study area**

104 The source region of the Yellow River is situated in the eastern QTP (Fig. 1a), covering
105 approximately 133,000 km², with elevations ranging from 2650 m to 6250 m. The mean annual
106 temperature in this area ranges between −3.5 and 7.5 °C. The annual average precipitation in this
107 area ranges from 420 to 705 mm, with the highest values occurring in the midstream region (Yang
108 et al., 2023). The dominant land cover consists of alpine meadows and alpine steppes (Fig. S1).
109 The area covers extensive permafrost and seasonally frozen ground, together covering more than
110 85% of the region (Z. Li et al., 2025; Yang et al., 2025). Under the combined influence of climate
111 warming and anthropogenic disturbances, permafrost in the upper reaches of the Yellow River
112 source region has shown a significant trend of degradation in recent decades (Yang et al., 2023).
113 The headwater region of the Yellow River (defined as upstream Xunhua (M4) in this study, which
114 is located on the edge of the Tibetan Plateau) contains a dense network of tributaries with annual
115 average discharge of 1.85×10^{10} m^3 during 1987-2016. Because damming affects the hydrology
116 downstream of Tangnaihai (M2), the discharge at M2 is considered representative of the study
117 area's natural discharge in our study. Within the national surface water quality monitoring network,
118 four sites (M1–M4, Maqu, Tangnaihai, Longyangxia, and Xunhua) are situated at the headwaters
119 of the Yellow River (Fig. 1b). In this study, the upstream (source to Deang), midstream (Deang to
120 Longwu), and downstream sections (Longwu to Xunhua) of the Yellow River's source region are
121 divided based on their geographical characteristics and are labeled B1(source-C1), B2 (C1-C2),
122 and B3 (C2-C3) (Fig. 1).

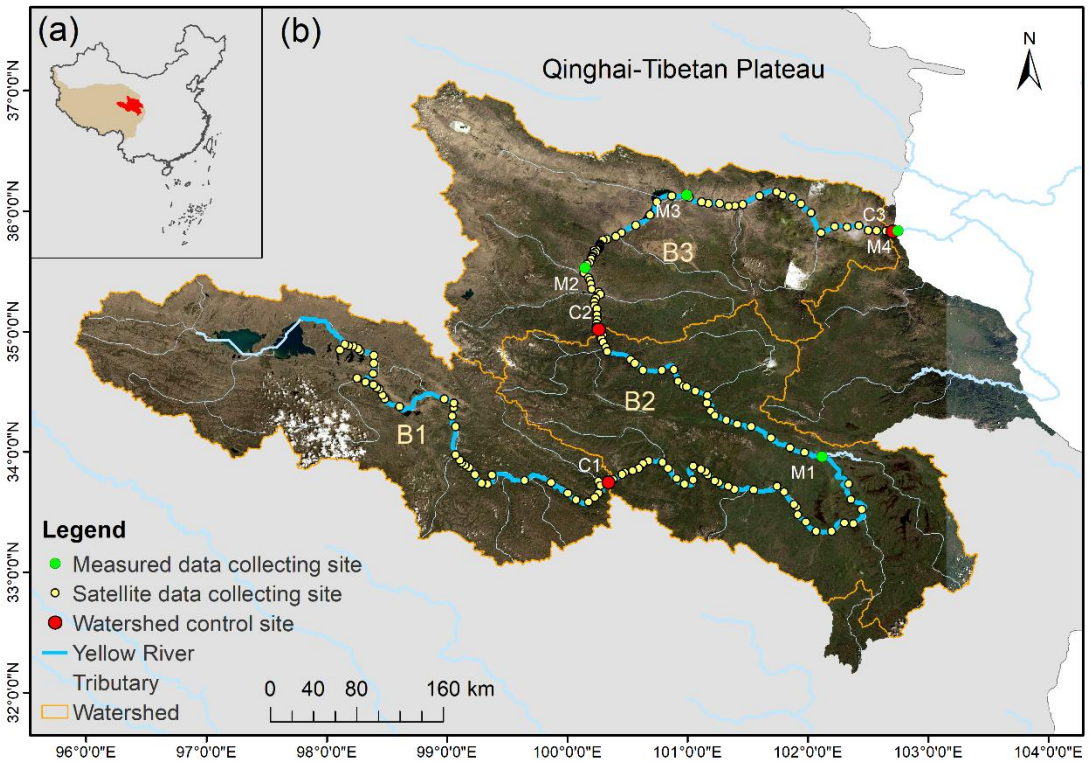


Fig.1 Location of the source region of the Yellow River (a), river network within the study area and data collection sites along the mainstream of the Yellow River (b). B1–B3 represent the upstream (source -C1), midstream (C1-C2), and downstream (C2-C3) region of the Yellow River's headstream in this study. A total of 160 monitoring sites span from downstream to upstream, with Site 1 located at the basin outlet.

2.2 Data collection

2.2.1 In-situ water quality data

Riverine COD_{Mn} data for model training were obtained from 107 monitoring sites distributed across the QTP and surrounding regions (Fig. S2), including four sites (M1–M4) positioned along the mainstream of the Yellow River (Fig. 1b). COD_{Mn} data for each site was obtained from the China National Environmental Monitoring Centre (CNEMC; https://www.cnemc.cn/) for the period 2021–2023. Measurements were performed every four hours (00:00, 04:00, 08:00, 12:00,

16:00, and 20:00). Following the *Environmental Quality Standards for Surface Water* (GB 3838–2002), COD_{Mn} was determined using the acidic potassium permanganate method, in which 50 ml water sample was oxidized by standardized $KMnO_4$ solution under controlled heating conditions. After the reaction, the residual permanganate was titrated, and COD_{Mn} was calculated from the amount of $KMnO_4$ consumed.

2.2.2 Satellite reflectance data

Surface reflectance data for model training was acquired for the 107 monitoring sites across the QTP and its surrounding areas from 2021 to 2023 using the Google Earth Engine (GEE) platform, based on Landsat-8 OLI/TIRS and Landsat-9 OLI-2/TIRS-2 imagery. For historical COD_{Mn} estimation in the source region of the Yellow River, surface reflectance data from Landsat-8/9 OLI/TIRS was also collected for 2014–2024 at 160 sites located at the headwater of the Yellow River (Fig. 1b). The Landsat-8/9 OLI datasets include five visible and near-infrared (VNIR) bands and two shortwave infrared (SWIR) bands. Atmospheric correction for Landsat-8/9 imagery was performed using the Land Surface Reflectance Code (LaSRC, v 1.5.0). Surface reflectance was extracted within a 90 m buffer around each site, and only pixels classified as water were retained. A minimum of 3×3 water pixels was required for a site–date matchup to be included. Pixels affected by clouds, cloud shadows, snow, ice, or non-water surfaces were removed based on the Landsat reflectance quality assessment bands.

2.2.3 Geographical feature data

Monthly precipitation and temperature data were obtained from the 1-km *Monthly Precipitation Dataset for China* (1901–2024) (Peng, 2025a, 2025b). Surface soil properties, including soil texture, pH, soil organic carbon, and bulk density, were extracted from the *Harmonized World Soil*

Database (Food and Agriculture Organization of the United Nations, 2021). Vegetation coverage data were sourced from the *China Regional 250-m Fractional Vegetation Cover Dataset* (2000–2024) (Gao et al., 2025). Land use data were derived from the *Land Use Dataset of China* (1980–2015) provided by the Resource and Environmental Science Data Center, Chinese Academy of Sciences (2020). Human Activity Intensity Index (HAII) were obtained from the *Human Activity Intensity Dataset of the Qinghai–Tibet Plateau* (2000–2020) (Liu, 2023). The Human Activity Intensity Index was calculated based on key human activity data, including agricultural and animal husbandry practices, industrial and mining development, urbanization, tourism, major ecological engineering projects, and pollutant discharge. Digital Elevation Model (DEM) data were retrieved from https://viewfinderpanoramas.org. Historical discharge data at C1, M1, M2 and M4 were compiled from multiple published sources (Wang, 2024; Liu et al., 2025), which are based on in-situ measurements from the same gauging network, and different sources were used to obtain complementary data. Future discharge projections were obtained from a single study and include the SSP126, SSP245, and SSP585 scenarios (M. Ma et al., 2023).

Future monthly temperature and precipitation data with spatial resolution of 1 km in the Yellow River source region were obtained from climate projections (Hu et al., 2025). This data was generated and bias corrected under three Shared Socioeconomic Pathways (SSPs) aligned with climate scenarios: SSP126 (sustainability-focused, low radiative forcing), SSP245 (intermediate, moderate stabilization), and SSP585 (fossil-fueled development, high radiative forcing).

2.3 Model development for historical COD_{Mn} reconstruction

2.3.1 Matching measured COD_{Mn} with satellite reflectance

COD_{Mn} data and satellite reflectance data (Landsat-8 OLI/TIRS and Landsat-9 OLI-2/TIRS-2) acquired from 107 sites across the eastern QTP and adjacent regions during 2021–2023 were used for model development (Fig. S2). Since Landsat-8/9 overpasses the study region at approximately 10:30 local time, COD_{Mn} measurements obtained at 08:00 or 12:00 on the same day were paired with corresponding satellite scenes. When multiple valid matches were available, only the 12:00 COD_{Mn} measurement was retained to ensure temporal consistency. A total of 3048 valid COD_{Mn}–reflectance matchups were obtained for the 107 sites during 2021–2023. These matched datasets covered a broad COD_{Mn} concentration range (0.25–23.2 mg L^{-1}) and were used to develop models for COD_{Mn} prediction.

2.3.2 Input and prediction variables of models

The 3048 valid COD_{Mn}–reflectance matchups were further processed to generate input variables. Input features included raw spectral bands and derived indices, with COD_{Mn} serving as the prediction variable. The raw spectral bands comprised Landsat-8/9 reflectance from Bands 1–7 and selected band ratios (SR_{nir}/SR_{red}, SR_{red}/SR_{green} and SR_{red}/SR_{blue}). Additionally, several spectral indices known to be sensitive to organic matter were calculated (Table S1), namely the Normalized Difference Chlorophyll Index (NDCI), Organic Carbon Index (OC_Index), Normalized Suspended Material Index (NSMI), and Hue Angle (Yan et al., 2025). Longitude and latitude were also incorporated as input variables.

2.3.3 Model training

AutoGluon is an open-source automated machine learning (AutoML) framework that builds high-accuracy predictive models for tabular data through multi-layer model ensembling and stacking. AutoGluon's *TabularPredictor* was configured in regression mode and trained using

multiple base learners (e.g., Gradient Boosting Machines, Random Forests, Neural Networks). The framework automatically optimized model selection, hyperparameters, and ensemble weights. Therefore, models for COD_{Mn} prediction were trained on Landsat-derived spectral features using AutoGluon-Tabular (v1.3.1) via its Python API in Python 3.8.3. The matched dataset (3048 pairs) described in Section 2.3.2 was randomly divided into training (80%) and testing (20%) subsets. A total training time limit of 600s was assigned to ensure sufficient exploration of model configurations.

2.3.4 Model evaluation

Model performance was evaluated using the negative Root Mean Squared Error (RMSE) for both the validation and test datasets (Eqs. 1–2). Lower (i.e., closer-to-zero) test and validation scores indicated superior model performance. The performance metrics for all models are summarized in Table S2.

$$RMSE = \sqrt{\frac{1}{n}\sum_{i=1}^{n}(y_i - \hat{y}_i)^2} \quad (1)$$

$$\text{Test /Validation score} = -RMSE \quad (2)$$

where, N denotes the size of the observations and y_i and $\hat{y}_i$ denote the in-situ values and satellite-retrieved values, respectively.

The importance of different input variables affecting the prediction of COD_{Mn} was also assessed based on the importance scores (Eq.3).

$$Importance\ (f_i) = M(D) - M(D_{_shuffled(f_i)}) \quad (3)$$

where, $M(\cdot)$, model performance metric (e.g., accuracy, log-loss, RMSE); D, original evaluation dataset; $D_{shuffled(fi)}$, same dataset, but with feature f_i randomly permuted; $Importance(fi)$, Drop in performance when f_i is destroyed.

2.3.5 Reconstruct of historical COD_{Mn}

The model exhibiting the highest test and validation scores was applied to reconstruct COD_{Mn} concentrations at 160 sites located in the headwater region of the Yellow River from 2014 to 2024 using Landsat-8 surface reflectance data. To evaluate model applicability and reliability, the reconstructed COD_{Mn} concentrations were compared with in situ measurements at two representative headwater sites. Two sites (M2 and M3) with abundant matched simulated and in-situ observations were selected to demonstrate the model's site-specific accuracy using the Mean Absolute Percentage Difference (MAPD), RMSE, and Bias, following the approach of Yan et al. (2025). Historical COD_{Mn} trends between 2014 and 2024 were assessed using the Mann–Kendall test and quantified using Sen's slope.

2.4 Prediction of future COD_{Mn} and its changes in the headstream of the Yellow River

To predict future COD_{Mn} levels at 160 sites in the headwaters of the Yellow River, the machine learning approach was also employed to model the relationships between geographical variables and the satellite-based estimates of COD_{Mn} levels. Soil texture (sand, silt, clay), bulk density, soil organic carbon, soil pH, altitude, human activity intensity, vegetation cover, land use, and ten-year averages of annual mean precipitation and temperature for each site during 2014-2024 were used as input features, while the ten-year average COD_{Mn} concentration for each site during 2014-2024 served as the target variable. The best-performing model, selected based on test and validation scores, was then used to predict future COD_{Mn} concentrations, incorporating both static variables (e.g., soil properties, vegetation cover, land use) and dynamic variables (future annual mean precipitation and temperature), depending on data availability. The projected future COD_{Mn} was model-based scenario projections conditional on the spatial stationarity assumption rather than

independently validated forecasts. Therefore, the selected model was used to learn the spatial relationships between geographical/environmental characteristics and Landsat-derived COD_{Mn} estimates, rather than directly learning an observed COD_{Mn} response. Satellite-based COD_{Mn} estimates, rather than directly observed COD_{Mn} measurements were used in this model, prediction uncertainty from the first-stage remote-sensing model can propagate into this model.

In order to predict the future COD_{Mn} using the trained model, future monthly temperature and precipitation data was collected from Hu et al. (2025). The bias correction was performed by using the delta Change Method (Text S1) to reconcile differences in temperature and precipitation data sources (Beyer et al., 2020; Cao et al., 2026). Future annual mean precipitation and temperature were then calculated for 2025-2040, 2041-2070, and 2071-2100, representing near-, mid-, and long-term horizons. Future COD_{Mn} changes in the Yellow River source region for 2025-2040, 2041-2070, and 2071-2100 under SSP126, SSP245, and SSP585 scenarios were calculated relative to the mean values from 2014–2024.

2.5 Calculation of COD_{Mn} and DOC flux

The COD_{Mn} flux in the source region of the Yellow River was calculated using Eq. 4:

$$F = C_i \times Q_i / 10 \quad (4)$$

where, F (Gg), nutrient export; C_i (mg/L), COD_{Mn} concentration at site i; Q_i (10^8 m³), river discharge at site i. The DOC flux was calculated from the DOC–COD_{Mn} relationship in rivers across China, expressed as $1.32F$ (Shang et al., 2026).

3 Results

3.1 Performance of developed models

3.1.1 Predicting historical COD_{Mn} using Landsat reflectance data

A total of 24 models were developed and evaluated to predict COD_{Mn} levels from Landsat reflectance data, with test and validation scores summarized in Table S2. The LightGBMLarge model demonstrated the highest predictive accuracy for COD_{Mn} across the QTP and surrounding regions, achieving test and validation scores of –0.22325 and –0.66913, respectively. Predicted versus in-situ measured COD_{Mn} levels for 2021–2023 based on training dataset are shown in Fig. 2a, with RMSE and R^2 of 0.326 and 0.925, respectively, indicating strong predictive performance.

The relative importance of input variables in the LightGBMLarge model was quantified using importance scores (Fig. 2b). The five most influential predictors were longitude, latitude, SR_{Red}/SR_{Green}, NSMI, and Band 1. Based on its performance, the LightGBMLarge model was selected to estimate historical COD_{Mn} levels in the source region of the Yellow River.

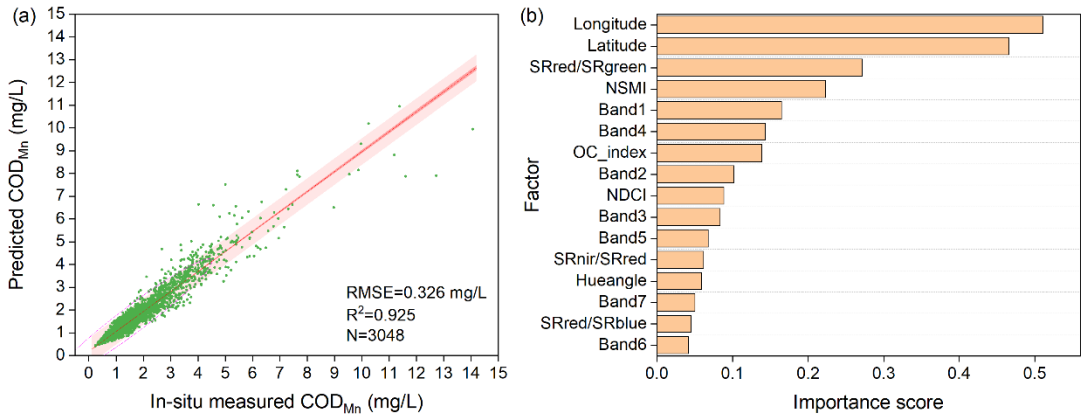


Fig.2 Model performance for COD_{Mn} prediction based on training set using Landsat 8/9 reflectance data (a), and importance of input variables in COD_{Mn} prediction (b).

To present a clearer site-level model reliability, two representative sites (M2 and M3) in the Yellow River headwaters were used to compare modeled and in-situ COD_{Mn} time series (Fig. 3). The results indicate that the model can accurately capture both spatial and temporal variability of riverine COD_{Mn} in the headstreams of the Yellow River. At site M3, RMSE, MAPD, and Bias

were 0.12 mg L^{-1}, 8.16%, and –2.38%, respectively, and RMSE, MAPD, and Bias at site M2 were 0.58 mg L^{-1}, 15.32%, and –2.23%, respectively.

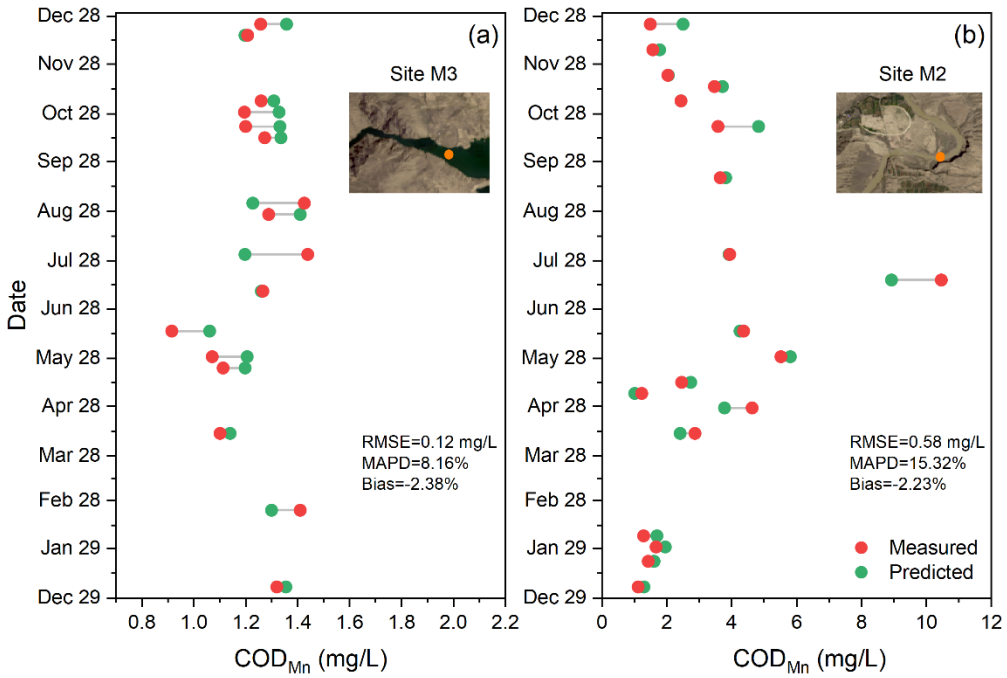


Fig.3 Comparison between predicted and measured COD_{Mn} values in 2023 at sites M3 (a) and M2 (b) within the Yellow River source region.

3.1.2 Prediction of future COD_{Mn} using geographical features

A total of 36 models for predicting future COD_{Mn} based on geographical features were evaluated (Table S3), and the LightGBMLarge model exhibited the highest performance, with test and validation scores of –0.081 and –0.264, respectively. Predicted versus satellite-based estimates of average COD_{Mn} levels based on the training dataset in the Yellow River source region are presented in Fig. 4a, achieving an R^2 of 0.913 and an RMSE of 0.177, indicating strong predictive capability of this model. Analysis of feature importance revealed that altitude, precipitation, temperature, and vegetation contributed most significantly to COD_{Mn} variability in the study area (Fig. 4b).

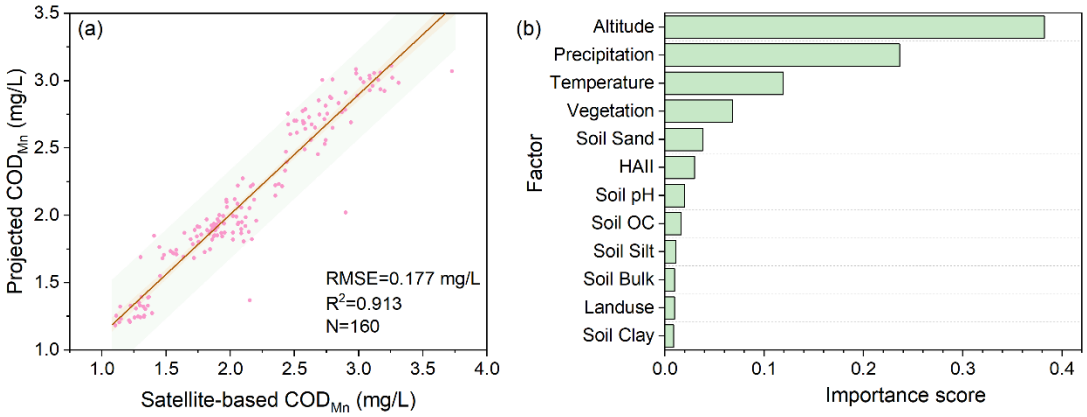


Fig.4 Performance of the developed model for COD_{Mn} prediction based on the training set using geographical feature data (a), and importance of variables in the predictive model (b). HAII is Human Activity Intensity Index; Soil OC represents soil organic carbon; Soil Bulk is soil bulk density; Soil Sand, Clay and Silt are soil texture.

3.2 Spatiotemporal changes of COD_{Mn} in the headstream of the Yellow River

The developed model estimated an annual mean COD_{Mn} concentration of 2.14 ± 1.06 mg L^{-1} in the Yellow River source region from 2014 to 2024, with pronounced spatial variability. In the upstream area, the mean COD_{Mn} was 1.89 ± 0.81 mg L^{-1}, while higher concentrations were observed in the mid-downstream region (2.73 ± 1.63 mg L^{-1}). The downstream area, which includes large reservoirs such as Longyangxia and Lijiaxia, exhibited significantly lower COD_{Mn} levels (1.54 ± 0.50 mg L^{-1}) (Fig. 5a, b).

Over the past decade, the midstream region showed a clear increasing trend in COD_{Mn}, with an average rise of 0.575 mg L^{-1} (Fig. 5c, d). In contrast, the upstream area exhibited both increasing and decreasing trends, with a mean change of 0.076 mg L^{-1}, whereas COD_{Mn} concentrations in the downstream region remained relatively stable (mean change: –0.099 mg L^{-1}). However, the historical COD_{Mn} trend was not statistically significant in the headwater region of

the Yellow River (Fig. S3).

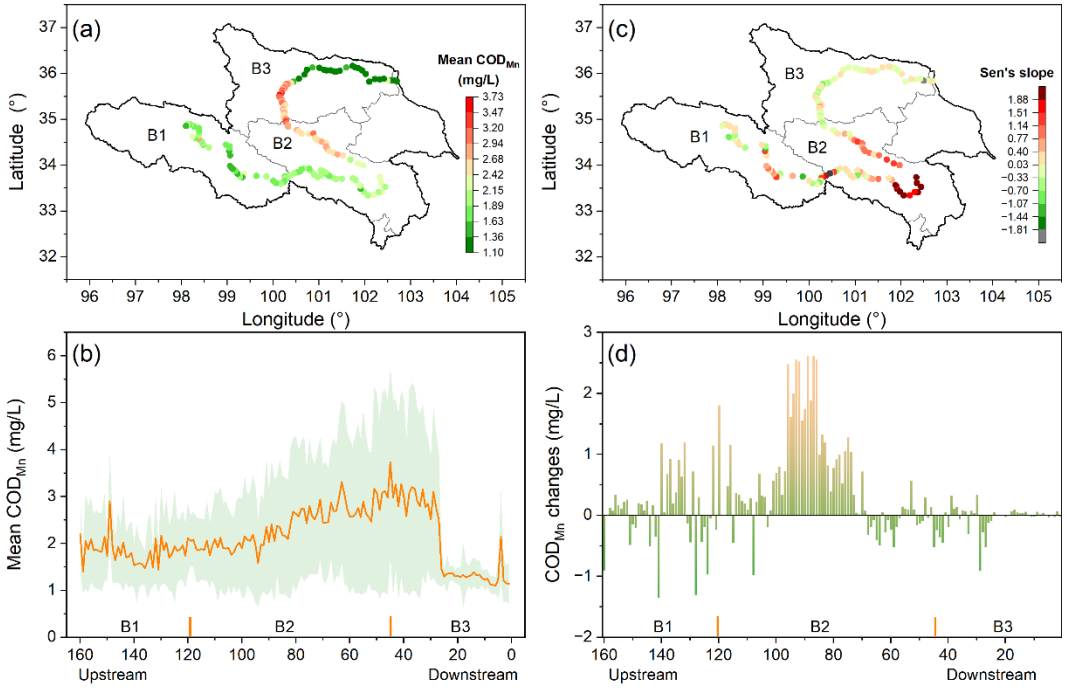


Fig.5 Spatial variation of mean COD_{Mn} (a, b), Sen's slope per decade for historic COD_{Mn} trend (c), and COD_{Mn} changes during 2014–2024 (d) in the Yellow River source region. Historic COD_{Mn} trend during 2014-2024 was assessed using the Mann–Kendall test and quantified using Sen's slope (mg COD_{Mn} L^{-1} $decade^{-1}$).

Seasonal variations of COD_{Mn} were also evident during our study. Average monthly COD_{Mn} concentrations ranged from 0.8 to 8 mg L^{-1} (Fig. 6). The downstream site maintained low (0.8-2.4 mg L^{-1}) and showed higher COD_{Mn} levels in summer (Fig. 6a), while the midstream site exhibited a pronounced increase from March, peaking in July (~8 mg L^{-1}), followed by a gradual decline (Fig. 6b). The upper–midstream site displayed two distinct peaks in late spring and summer, suggesting episodic organic inputs associated with ice melt and rainfall (Fig. 6c). Upstream sites remained low to moderate (1-3 mg L^{-1}) with minimal seasonal variation (Fig. 6d).

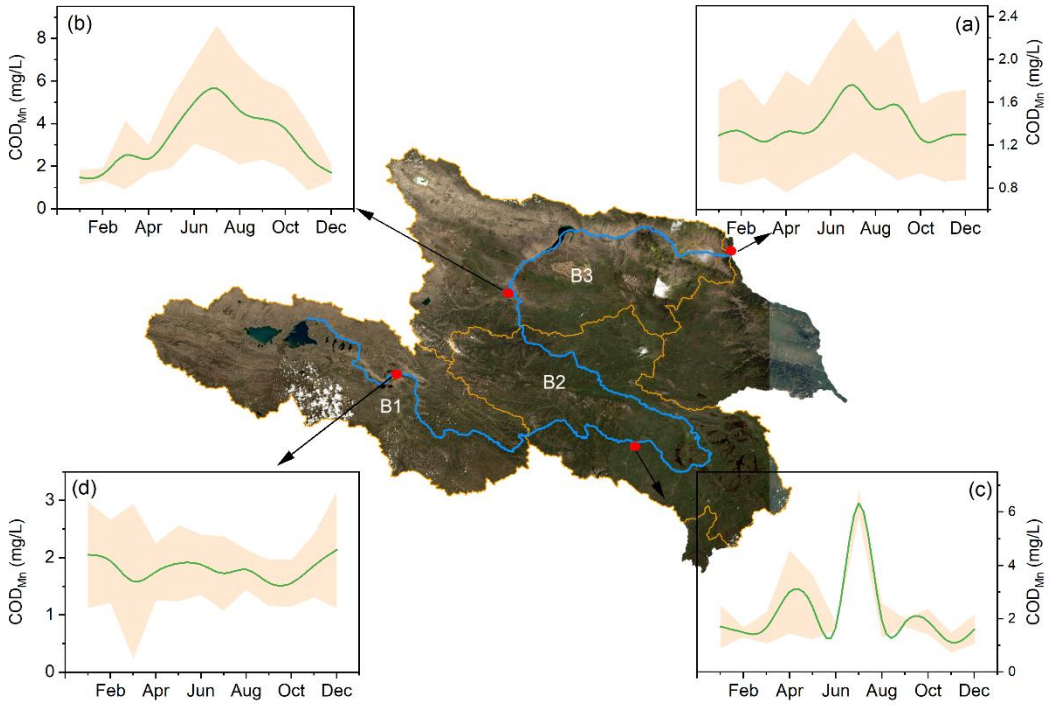


Fig.6 Averaged monthly variations of COD_{Mn} during 2014–2024 within the Yellow River source region.

3.3 Future climate and COD_{Mn} changes in the source region of the Yellow River

Across all scenarios and periods, precipitation exhibits a consistent spatial pattern, increasing from upstream reaches to a midstream maximum and subsequently decreasing toward downstream sections (Fig. 7a-c). This pattern is preserved under all SSPs, although the magnitude of precipitation varied among scenarios and time slices. Relative to current conditions, precipitation increases slightly in the midstream region under SSP126 and SSP245, particularly during the mid- and late-century periods. Under SSP585, precipitation displays enhanced increase, with higher midstream values during 2041–2070 and 2071–2100 and lower precipitation toward downstream reaches.

Compared with current conditions, future temperature rises across the entire study area (Fig.

7d-f), with the magnitude of warming increasing over time and from SSP126 to SSP585. Under SSP126, temperature increases are relatively moderate, whereas SSP245 shows stronger warming, especially during 2071–2100. The largest temperature increases occurred under SSP585, with pronounced downstream variability during the late-century period, resulting in an amplified longitudinal temperature gradient.

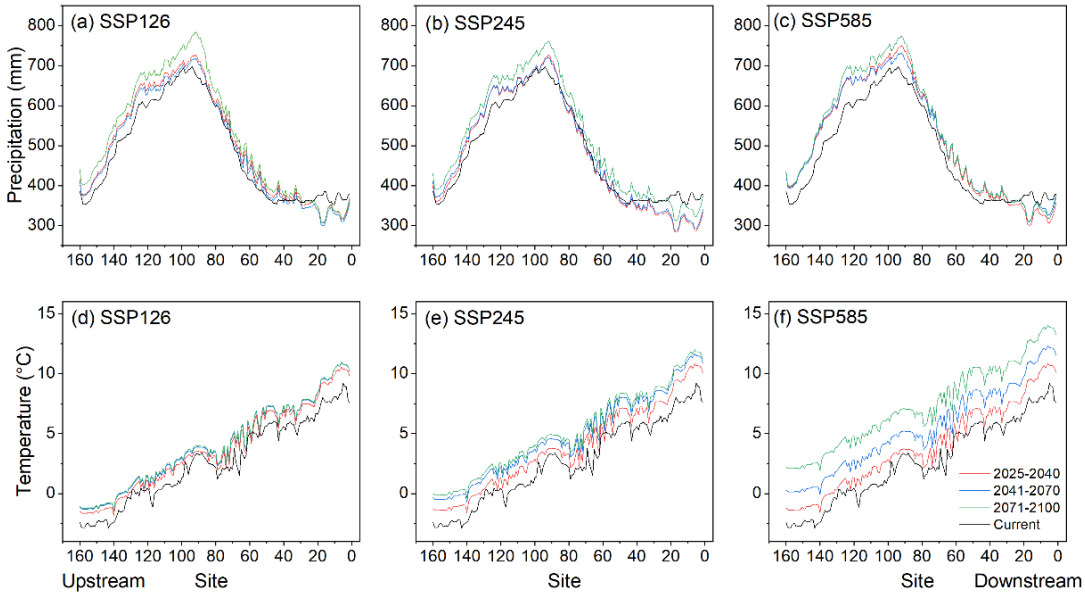


Fig.7 Projected precipitation and temperature variations for 2025-2040, 2041-2070, and 2071-2100 under SSP126, SSP245, and SSP585 scenarios.

Projected changes in COD_{Mn} across the study area show pronounced spatial and temporal variability under all three scenarios (Fig. 8). During the near-term period (2025–2040), COD_{Mn} changes are generally modest, with most monitoring sites exhibiting values close to zero. In the mid-term period (2041–2070), the COD_{Mn} changes show an overall increase, with mean value of 0.05 mg L^{-1}. Specifically, midstream sites more frequently experience decreases in COD_{Mn}, whereas upstream and downstream regions display a mixture of small increases and decreases. By the late-century period (2071–2100), the average change in COD_{Mn} is -0.01 mg L^{-1}. COD_{Mn} shows

a pronounced decrease trend in the midstream area (-0.12 mg L^{-1}) under SSP585. Upstream and downstream areas show a higher occurrence of positive COD_{Mn} changes. Overall, COD_{Mn} shows a slight increasing trend across the three scenarios over different periods, with 877 positive changes (61%) and 563 negative changes (39%).

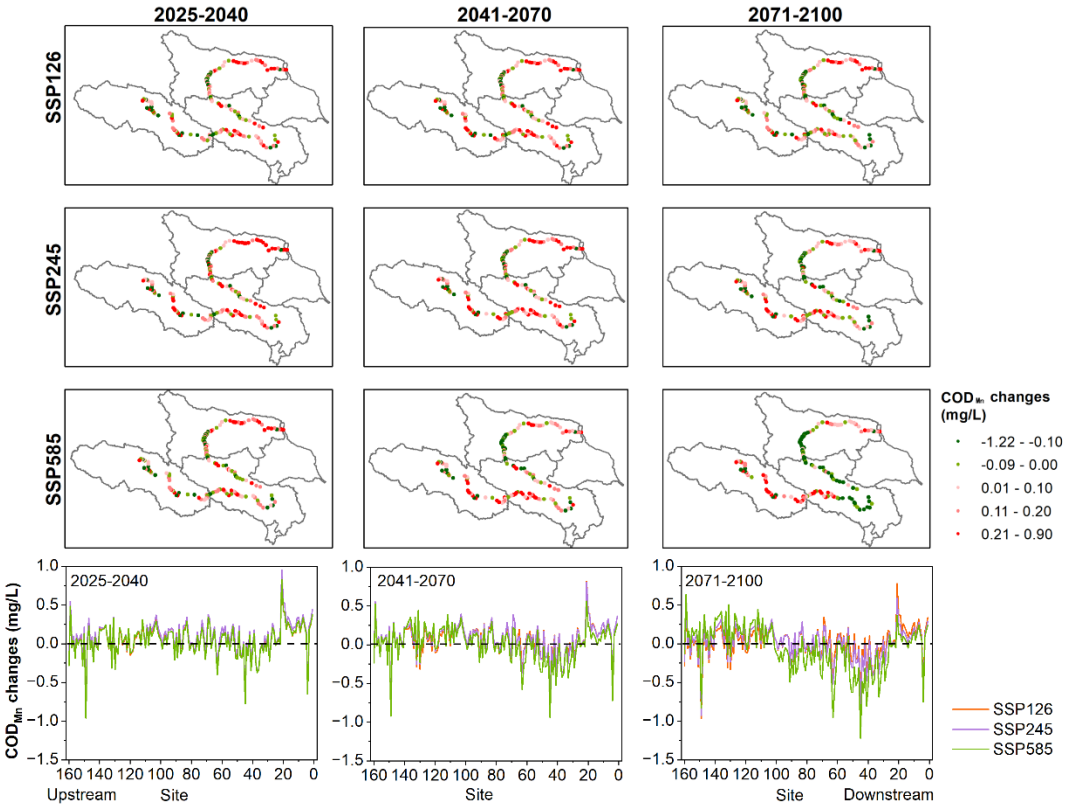


Fig.8 Projected spatial variation of COD_{Mn} changes in the Yellow River source region for 2025-2040, 2041-2070, and 2071-2100 under SSP126, SSP245, and SSP585 scenarios. COD_{Mn} changes were calculated relative to the mean values from 2014–2024.

3.4 Historical and future riverine organic matter exports

Historical and future COD_{Mn} and converted DOC exports are shown in Fig. 9 and Fig. S4, respectively. Based on the annual average discharge at control site M4 (1987–2021), approximately 28.1 Gg of COD_{Mn} (37.1 Gg DOC) was exported from the entire study area. In

contrast, the annual mean COD_{Mn} export at site M2 was 62.5 Gg (82.5 Gg DOC), indicating that approximately 34 Gg of COD (44.8 Gg DOC) was either deposited or decomposed between M4 and M2 along the downstream of the Yellow River's source region. The export of riverine organic matter primarily occurred during the wet season (June–October) (Fig. 9a, S4a), which contributes substantially to the annual dissolved organic matter export from the source region (Fig. 9b, S4b). Additionally, the observed increase in COD_{Mn} or DOC export between sites M1 and M2 highlights the midstream region as a major source of dissolved organic matter (Fig. 9b, S4b).

Though the projected discharge presents an overall increase trend (Fig. 9c), the calculated future COD_{Mn} (or DOC) export at site M2 indicates a slight declining trend under the three scenarios (Fig. 9d, S4c). For example, the average COD_{Mn} export at M2 under different scenarios is expected to decrease from 62.5 Gg to 59.6 Gg (82.5 Gg to 78.7 Gg DOC) by 2100.

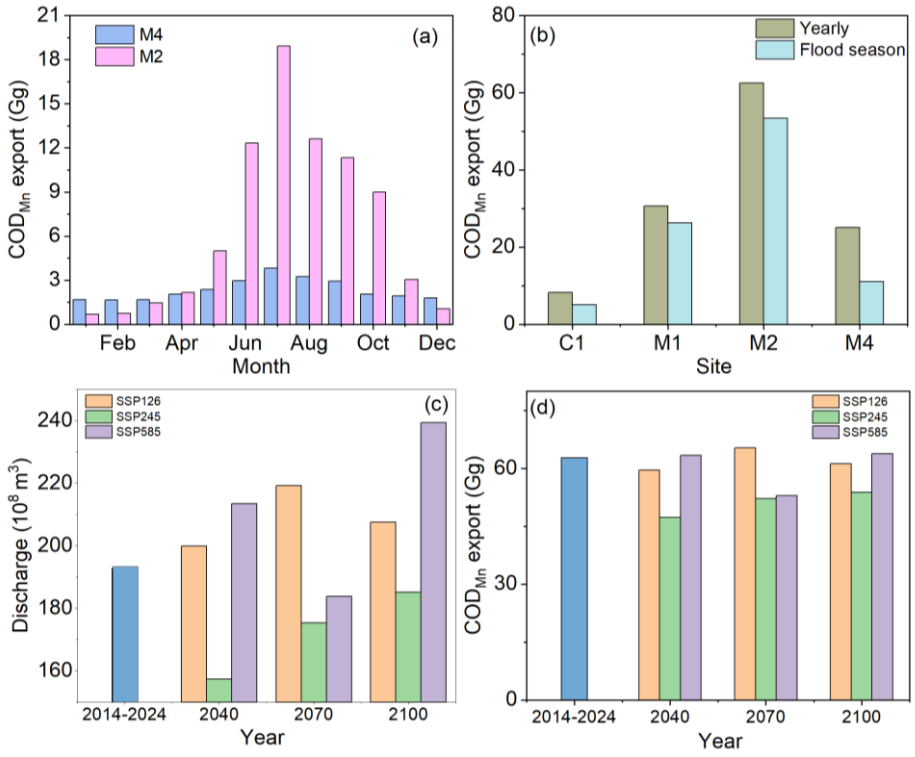


Fig.9 Monthly average COD_{Mn} export at sites M2 and M4 during 2014-2024 (a); comparison between annual and flood-season COD_{Mn} exports (b); projected annual average discharge

391 collected from Ma et al. (2023) (c), and projected COD_{Mn} export at M2 for 2040, 2070, and 2100
392 under SSP126, SSP245, and SSP585 scenarios (d).
393
394 **4 Discussion**
395 **4.1 Factors driving riverine organic matter dynamics in the headstream of the Yellow River**
396 **4.1.1 Spatial variations**
397 Primary sources of riverine organic carbon include losses from soils, plant litter, root exudates in
398 grasslands, and permafrost thaw via surface runoff (Yan et al., 2023). In this study, precipitation,
399 temperature, vegetation, and soil texture were identified as key drivers of COD_{Mn} variation (Fig.
400 4b). Notably, the overall soil organic carbon, vegetation cover, fine particle content, and
401 precipitation are higher in the midstream region of the headwater (Fig. S5), providing abundant
402 carbon sources and facilitating transport to nearby rivers, resulting in elevated COD_{Mn} levels and
403 fluxes in the mid-downstream areas (Figs. 5a, 9a, b). Additionally, bare land in the
404 mid-downstream areas of the headstream may also contribute to the soil erosion and the associated
405 organic carbon losses (Fig. S1). L. Li (2025) identified the higher lateral fluxes of river organic
406 matter in the midstream area of the Yellow River' s source region. Consequently, the midstream
407 area represents a critical source of organic carbon for the Yellow River headwaters.
408 In contrast, COD_{Mn} levels decreased markedly in the downstream region (Figs. 5a, b). This
409 decline is likely driven by damming, as three large reservoirs, Longyangxia, Laxiwa, and Lijiaxia
410 have been constructed in the downstream headwater region since the 1970s. Reservoirs increase
411 water residence time, promoting deposition and decomposition of organic carbon, greenhouse gas
412 emissions, and uptake by aquatic plants (Maavara et al., 2017, 2020). Therefore, the deposition or

decomposition of organic matter along the downstream areas may contribute to the decline of COD_{Mn} levels. The deposition of riverine organic matter can be inferred from the decrease in COD_{Mn} (or DOC) fluxes at the outlet (M4) of the study area relative to site M2 (Figs. 9, S4). L. Li et al. (2025) also reported negative dissolved organic matter fluxes in the main channels of the Yellow River's headstreams. Additionally, the decomposition of the deposited organic matter is evidenced by CO_2 outgassing from the river water. Previous study has found that CO_2 outgassing from the cascade reservoirs of Yellow River's source region was estimated at 131 ± 156 mmol m^{-2} d^{-1} in dry seasons and 466 ± 366 mmol m^{-2} d^{-1} in flood seasons (Wang et al., 2022). Therefore, these observations suggest that the sedimentation and degradation of organic matter contributes to lower COD_{Mn} concentrations in the downstream area.

The COD_{Mn} concentration remained relatively stable along the upper to middle reaches of the Yellow River's headwaters. This region is characterized by permafrost and seasonally frozen ground, with low precipitation and limited runoff (Yang et al., 2023). Surface runoff in this area primarily originates from precipitation, snowmelt, and glacier melt (G. Li et al., 2025). Consequently, due to the relatively uniform and stable runoff and land cover, COD_{Mn} levels exhibited a homogeneous spatial distribution along the upper to middle reaches of the Yellow River's headwaters.

4.1.2 Temporal variations

Climate-driven changes in runoff and temperature strongly influence catchment-scale carbon dynamics, altering riverine organic matter fluxes globally (Costa et al., 2023). Over the past decade, air temperature in the source region of the Yellow River has shown an increasing trend, with a basin–averaged increase of 0.67 °C, and the precipitation also presented an over increase

trend though decrease slightly after 2019 (Fig. S6). The study area is particularly sensitive to warming-induced permafrost thaw, glacier melting, soil erosion, and intensified human activities over recent decades (Chen et al., 2022; Deng et al., 2025; Lan et al., 2025), which modify organic matter sources and lateral transport between terrestrial and aquatic systems, affecting ROM levels and fluxes in rivers (Wang et al., 2020; Chen et al., 2022; S. Wang et al., 2025). For example, previous studies highlighted that permafrost thaw was projected to release 129 ± 21.02 Tg soil organic carbon annually (Lan et al., 2025). Glacier melting contributes an estimated 0.19 Tg C yr^{-1} as dissolved organic carbon (Chen et al., 2022). Intensified rainfall has increased soil erosion by 42% over the past four decades, resulting in an average soil carbon loss of 4 ± 1.2 Tg C yr^{-1} (Deng et al., 2025).

Therefore, affected by the increased temperature and precipitation, COD_{Mn} concentrations in the source region of the Yellow River exhibited an overall increasing trend over the past decade, with an average rise of 0.257 mg L^{-1} (Figs. 5c, d). Especially the midstream region experienced the most pronounced increase (0.575 mg L^{-1}). The higher precipitation combined with increased runoff likely enhance organic matter leaching from grasslands, contributing to the rise of riverine COD_{Mn} in the midstream area (Yang et al., 2023; Chen et al., 2025).

In addition to climate effects, growing human activities such as land use changes, grazing, and construction on the QTP also influence carbon mobilization (Chen et al., 2022). Human-induced land-use changes, grassland degradation, construction activities, and overgrazing can lead to organic matter losses in the study area. In addition, the construction and urbanization of natural and agricultural ecosystems may further accelerate organic matter losses within the watershed. All these human activities may contribute to the rising of COD_{Mn} in the headstream of

457 the Yellow River.

458 **4.2 Future riverine organic matter changes in the headstream of the Yellow River under**
459 **climate change**

460 Rapid climate change in alpine regions is altering carbon cycling in both terrestrial and aquatic
461 ecosystems (Chen et al., 2022). As carbon dynamics are highly sensitive to climatic variations,
462 warming and wetting trends are expected to influence the stability of riverine organic matter in
463 alpine catchments. Numerous studies indicate that precipitation and temperature on the QTP are
464 projected to increase throughout this century, particularly in high-elevation areas (Meng et al.,
465 2023; Karim et al., 2025). Our projections also suggest an overall increase in precipitation,
466 especially in the up-midstream area of the Yellow River source region (Fig. 7), and significant
467 warming is projected in the whole study area by 2100, especially under SSP245 and SSP585.
468 Climate-driven changes are expected to induce the largest variability in COD_{Mn} concentrations in
469 the midstream region (Fig. 8). COD_{Mn} levels are projected to increase in most parts of the source
470 region of the Yellow River, whereas annual average COD_{Mn} exports from the whole catchment
471 will decrease slightly from 62.5 Gg to 59.6 Gg (82.5 Gg to 78.7 Gg DOC) (Fig. 9d, S4c).

472 ROM dynamics are jointly regulated by organic matter supply and hydrological processes
473 within catchments (Li et al., 2022; Wu et al., 2024). Increased precipitation can enhance surface
474 runoff, leading to losses of organic matter from the catchment, and COD_{Mn} concentrations may be
475 diluted as discharge continues to increase. The projected warming in the headwater area of the
476 Yellow River will lead to the continuing permafrost degradation, promoting the loss of organic
477 matter within the catchment and leading to the increase of the COD_{Mn} level in the headstreams. In
478 addition, damming prolongs water residence time, promoting organic matter deposition in cascade

reservoirs in the downstream area of the Yellow River's source region and reducing the riverine organic matter export from the study area. Under warm conditions, the degradation of deposited organic matter in the bottom of the reservoir may be enhanced, releasing additional organic carbon from reservoir sediments and contributing to the rise of COD_{Mn} levels in the downstream area (Vachon et al., 2021; Battin et al., 2023).

However, the extent to which organic matter reaches rivers depends on hydrological processes and connectivity between the source region and river channels. The characteristics of rainfall events may shift the ROM response to storms from transport-limited to supply-limited, thereby reducing ROM levels (Li et al., 2022). Consequently, the projected increase in precipitation by the 2100s is expected to lead to a decrease in COD_{Mn} levels within the midstream areas (Fig. 8). In addition, permafrost thaw induced by the warming can also alter runoff pathways, promoting subsurface flow and potentially reducing surface discharge to rivers (Yang et al., 2023). Increased vegetation cover can also reduce transport of organic matter through reducing soil erosion and surface runoff (W. Ma et al., 2023; Liu et al., 2024). Therefore, the export of DOC from the headwaters of the Yellow River may remain stable or decrease slightly under the combined effects of climate change, hydrological variability, permafrost degradation, and human activities.

4.3 Uncertainty in riverine organic matter dynamics on the QTP

Understanding riverine organic matter dynamics is essential for assessing aquatic ecosystem feedback to climate change. Ongoing warming and wetting on the QTP are expected to alter carbon stability, increasing uncertainty in watershed organic matter losses (Bai et al., 2025). For instance, increased precipitation may enhance surface runoff, however, rising temperatures can

501 also decrease catchment runoff by enhancing evaporation. The influence of hydrological processes
502 on ROM dynamics depends on the characteristics of the catchment (Li et al., 2022). Previous
503 studies have predicted both increasing and decreasing streamflow trends on the QTP under future
504 climate scenarios (Yang et al., 2023; G. Li et al., 2025; San et al., 2025). Increased streamflow
505 may elevate COD_{Mn} in rivers, or dilute COD_{Mn} due to higher streamflow. Conversely, reduced
506 streamflow may decrease organic matter transport to rivers or concentrate COD_{Mn} in river water.
507 Additionally, warming-induced permafrost thaw may accelerate topsoil organic matter
508 mobilization, stimulate microbial activity, and promote soil organic matter decomposition,
509 releasing more dissolved organic matter (Ziliang Li et al., 2025). However, the frozen ground
510 degradation can also result in the decreased surface runoff by increasing the subsurface runoff
511 (Yang et al., 2023). Vegetation greening on the QTP may both enhance soil carbon storage and
512 reduce organic matter losses to river networks through mitigating soil erosion (Deng et al., 2025).
513 Therefore, climate change can further differentially affect terrestrial carbon stocks and carbon
514 losses, introducing additional complexity and uncertainty in catchment-scale organic matter
515 sources and transport (Chen et al., 2022; W. Ma et al., 2023; Liu et al., 2024).
516 In-stream carbon biogeochemical processes are also highly complex under changing climatic
517 conditions. Organic matter decomposition depends on temperature, redox conditions, hydrology,
518 microbial activity, and organic matter characteristics (Battin et al., 2023). The climate change is
519 projected to change the hydrological processes and the associated biogeochemical processes,
520 further altering the carbon cycling in the alpine rivers. However, interactions among these factors
521 are not fully understood in alpine rivers, making predictions of alpine river metabolism and carbon
522 budget under climate change uncertain (L. Li et al., 2025).

Anthropogenic activities on the QTP further contribute to uncertainty. Warming and wetting may expand farming, increasing soil erosion and carbon losses (Chen et al., 2022). Future dam construction alters organic matter transport by promoting deposition, influencing greenhouse gas emissions, and facilitating organic matter degradation (Battin et al., 2023). Conversely, ecological restoration, such as afforestation, can increase soil organic matter accumulation and litterfall (Chen et al., 2022; Yan et al., 2023), leading to increase in organic matter and the COD_{Mn} levels in the alpine Rivers.

4.4 Limitations of this study

In this study, we project a general increase in levels and fluxes of COD_{Mn} based on modeled temperature, precipitation, and discharge. However, future climatic trends may deviate from current projections, and the predicted temperature and precipitation may not represent the actual future patterns. Besides, our developed model does not incorporate changes in land covers, soil carbon stocks, hydrological processes, or in-stream carbon biogeochemistry, all of which may significantly influence riverine carbon cycling. Therefore, future research should integrate these factors to develop more precise, process-based models and improve understanding of carbon dynamics in alpine river catchments.

In addition, future COD_{Mn} projection model is trained on COD_{Mn} values predicted by the first-stage retrieval model rather than on independent long-term observations, so the two models are not statistically independent and retrieval errors inevitably propagate into the climate projections. The extrapolating spatial "geographical characteristics—COD_{Mn} concentration" relationships to temporal climate change represents a space-for-time substitution that assumes stationarity, an assumption that is difficult to test rigorously with the available data. Finally,

545 COD_{Mn} is an oxygen-equivalent index rather than a direct measure of organic matter or carbon.
546 The DOC export estimated in this study was derived from a simplified empirical relationship
547 between COD_{Mn} and DOC in rivers across China, which may introduce additional uncertainty into
548 the DOC estimates.

549 **5 Conclusions**

550 In this study, LightGBM-Large models were developed to reconstruct the historical variations of
551 COD_{Mn} in the source region of the Yellow River and to predict its future changes. Our findings
552 identify the midstream region of the Yellow River's headstream, with higher COD_{Mn} levels (2.73 ±
553 1.63 mg L^{-1}), is sensitive to climate change and exhibited an increasing trend of COD_{Mn} (0.575
554 mg L^{-1}) in the past decade. Precipitation and temperature were identified as the key factors
555 influencing COD_{Mn} dynamics in the headwaters of the Yellow River. Future projections suggest
556 that increased precipitation and temperature may lead to an overall rise of COD_{Mn} levels, with
557 decrease in some specific sites. The export of dissolved organic matter from the headwaters of the
558 Yellow River is projected to remain stable or decrease slightly in the future. However, the limited
559 spatial and temporal resolution of Landsat data and lack of geophysical data, still poses challenges
560 for accurately capturing rapid variations in riverine organic matter in the source region of the
561 Yellow River. Therefore, future research in alpine rivers should focus on developing more robust
562 models by integrating long-term and high-resolution satellite observations and in-situ observations
563 and incorporating a broader range of environmental variables.

564 **Data availability**

565 Water quality data in this study are obtained from the China National Environmental Monitoring
566 Centre (https://www.cnemc.cn). Historical monthly precipitation and temperature, surface soil

properties, vegetation coverage, and projected future monthly temperature and precipitation data are obtained from the Tibetan Plateau Data Centre (https://data.tpdc.ac.cn). The modeled historical and projected future COD_{Mn} data in this study are openly available on Zenodo (https://doi.org/10.5281/zenodo.22766232).

Author contributions

XW: Conceptualization, Methodology, Writing original draft, Funding acquisition; JW: Methodology, Data curation, Review and editing; TR: Investigation, Formal analysis, Validation; JZ: Validation, Conceptualization, Review and editing.

Competing interests

The authors declare that they have no conflict of interest.

Acknowledgments

We thank the National Tibetan Plateau/Third Pole Environment Data Center (TPDC) for providing the environmental data, and Google Earth Engine (GEE) for the river surface reflectance data used in this study.

Financial support

This work was funded by China West Normal University (22kA001) and the Natural Science Foundation of Sichuan Province (2026NSFSC0226).

References

Adegun, A., Viriri, S., Tapamo, J.-R., 2023. Review of deep learning methods for remote sensing satellite images classification: experimental survey and comparative analysis. Journal of Big Data 10. https://doi.org/10.1186/s40537-023-00772-x

Aryal, S., Pokhrel, Y., 2025. Spatio-temporal heterogeneities in hydrologic dynamics across the

589 Asian Water Tower. Journal of Hydrology 662, 133951.
590 https://doi.org/10.1016/j.jhydrol.2025.133951
591 Bai, Y., Peng, Y., Zhang, D., Yang, G., Chen, L., Kang, L., Zhou, W., Wei, B., Xie, Y., Yang, Y.,
592 2025. Heating up the roof of the world: tracing the impacts of in-situ warming on carbon
593 cycle in alpine grasslands on the Tibetan Plateau. National Science Review 12, nwae371.
594 Battin, T.J., Lauerwald, R., Bernhardt, E.S., Bertuzzo, E., Gener, L.G., Hall, R.O., Hotchkiss, E.R.,
595 Maavara, T., Pavelsky, T.M., Ran, L., Raymond, P., Rosentreter, J.A., Regnier, P., 2023. River
596 ecosystem metabolism and carbon biogeochemistry in a changing world. Nature 613, 449–
597 459. https://doi.org/10.1038/s41586-022-05500-8
598 Beusen, A.H.W., Doelman, J.C., Van Beek, L.P.H., Van Puijenbroek, P.J.T.M., Mogollón, J.M.,
599 Van Grinsven, H.J.M., Stehfest, E., Van Vuuren, D.P., Bouwman, A.F., 2022. Exploring river
600 nitrogen and phosphorus loading and export to global coastal waters in the Shared
601 Socio-economic pathways. Global Environmental Change 72, 102426.
602 https://doi.org/10.1016/j.gloenvcha.2021.102426
603 Beyer, R., Krapp, M., Manica, A., 2020. An empirical evaluation of bias correction methods for
604 palaeoclimate simulations. Clim. Past 16, 1493–1508.
605 https://doi.org/10.5194/cp-16-1493-2020
606 Cao, Y., Yao, H., Zhang, C., Gu, C., Yang, L., Hao, R., Li, X., Wang, Z., Xiao, H., Wang, J., Shi, Z.,
607 2026. Data-driven assessment of nitrogen and phosphorus buffering capacity across 460
608 Chinese watersheds: Spatial patterns, drivers, and future projections. Water Research 293,
609 125424. https://doi.org/10.1016/j.watres.2026.125424
610 Chen, H., Ju, P., Zhu, Q., Xu, X., Wu, N., Gao, Y., Feng, X., Tian, J., Niu, S., Zhang, Y., 2022.

611 Carbon and nitrogen cycling on the Qinghai–Tibetan Plateau. Nature Reviews Earth &
612 Environment 3, 701–716.
613 Chen, Y., Xu, C., Liu, Wenjun, De Boeck, H.J., Zhou, H., Chen, Q., Ma, Y., Liu, Weihong, Zhao,
614 L., Wang, H., Chen, J., Zhang, Y., Zhang, Z., 2025. Machine learning-based assessment of
615 grassland degradation levels on the Qinghai-Tibet Plateau from 2000 to 2020. Ecological
616 Indicators 180, 114360. https://doi.org/10.1016/j.ecolind.2025.114360
617 Costa, D., Sutter, C., Shepherd, A., Jarvie, H., Wilson, H., Elliott, J., Liu, J., Macrae, M., 2023.
618 Impact of climate change on catchment nutrient dynamics: insights from around the world.
619 Environ. Rev. 31, 4–25. https://doi.org/10.1139/er-2021-0109
620 Deng, R., Li, D., Zhao, Y., Walling, D.E., Panagos, P., Borrelli, P., Ciais, P., Huang, Y., Bai, Y.,
621 Chalov, S., Golosov, V.N., Fu, X., Miao, C., Wei, J., Ni, J., 2025. Intensified rainfall overrides
622 vegetation greening in driving erosion and carbon loss on the Tibetan Plateau. Science
623 Bulletin. https://doi.org/https://doi.org/10.1016/j.scib.2025.09.005
624 Deng, Y., Zhang, Y., Pan, D., Yang, S.X., Gharabaghi, B., 2024. Review of Recent Advances in
625 Remote Sensing and Machine Learning Methods for Lake Water Quality Management.
626 Remote Sensing 16. https://doi.org/10.3390/rs16224196
627 Food and Agriculture Organization of the United Nations, I.I. for A.S.A., 2021. China soil map
628 based harmonized world soil database (HWSD) (v1.1) (2009). National Tibetan Plateau Data
629 Center.
630 Gao, J., Shi, Y., Zhang, H., Chen, X., Zhang, W., Shen, W., Xiao, T., Zhang, Y., 2025. China
631 regional 250m fractional vegetation cover data set (2000-2024). National Tibetan Plateau
632 Data Center. https://doi.org/10.11888/Terre.tpdc.300330

633 Giri, S., 2021. Water quality prospective in Twenty First Century: Status of water quality in major
634 river basins, contemporary strategies and impediments: A review. Environmental Pollution
635 271, 116332. https://doi.org/10.1016/j.envpol.2020.116332
636 Hong, J., Pang, B., Zhao, L., Shu, S., Feng, P., Liu, F., Du, Z., Wang, X., 2025. Soil phosphorus
637 crisis in the Tibetan alpine permafrost region. Nat Commun 16.
638 https://doi.org/10.1038/s41467-025-61501-x
639 Hu, M., Liu, Y., Zhang, Y., Shen, H., Yao, M., Dahlgren, R.A., Chen, D., 2020. Long-term (1980–
640 2015) changes in net anthropogenic phosphorus inputs and riverine phosphorus export in the
641 Yangtze River basin. Water Research 177, 115779.
642 https://doi.org/10.1016/j.watres.2020.115779
643 Hu, X., Shi, S., Zhou, B., Ni, J., 2025. A 1 km monthly dataset of historical and future climate
644 changes over China. Sci Data 12, 436. https://doi.org/10.1038/s41597-025-04761-y
645 Jiao, N., Liu, J., Edwards, B., Lv, Z., Cai, R., Liu, Y., Xiao, X., Wang, J., Jiao, F., Wang, R., Huang,
646 X., Guo, B., Sun, J., Zhang, R., Zhang, Y., Tang, K., Zheng, Q., Azam, F., Batt, J., Cai, W.-J.,
647 He, C., Herndl, G.J., Hill, P., Hutchins, D., LaRoche, J., Lewis, M., MacIntyre, H., Polimene,
648 L., Robinson, C., Shi, Q., Suttle, C.A., Thomas, H., Wallace, D., Legendre, L., 2021.
649 Correcting a major error in assessing organic carbon pollution in natural waters. Science
650 Advances 7, eabc7318. https://doi.org/10.1126/sciadv.abc7318
651 Karim, R., Li, S., Su, T., Ayugi, B.O., Babaousmail, H., Xiao, S., 2025. Future Climate Changes
652 on the Qinghai–Tibetan Plateau Under CMIP6 Global Climate Models. International Journal
653 of Climatology e70005.
654 Kotlarski, S., Gobiet, A., Morin, S., Olefs, M., Rajczak, J., Samacoïts, R., 2023. 21st Century

alpine climate change. Clim Dyn 60, 65–86. https://doi.org/10.1007/s00382-022-06303-3

Lan, T., Ma, Q., Lai, Y., Zhang, M., Harbor, J., Luo, X., 2025. Quantifying the water contributions and carbon consequences of permafrost degradation on the Tibetan Plateau. Science Bulletin. https://doi.org/https://doi.org/10.1016/j.scib.2025.09.029

Li, G., Li, Zongxing, Zhang, B., Li, Zongjie, 2025. Changes in runoff from major alpine watersheds on the Qinghai-Tibetan plateau: A review. Journal of Hydrology: Regional Studies 60, 102514. https://doi.org/https://doi.org/10.1016/j.ejrh.2025.102514

Li, J., Wang, G., Song, C., Sun, S., Ma, J., Wang, Y., Guo, L., Li, D., 2024. Recent intensified erosion and massive sediment deposition in Tibetan Plateau rivers. Nat Commun 15, 722. https://doi.org/10.1038/s41467-024-44982-0

Li, J., Wang, G., Sun, S., Ma, J., Guo, L., Song, C., Lin, S., 2025. Mapping and reconstruct suspended sediment dynamics (1986–2021) in the source region of the Yangtze River, Qinghai-Tibet Plateau using Google Earth Engine. Remote Sensing of Environment 317, 114533. https://doi.org/https://doi.org/10.1016/j.rse.2024.114533

Li, L., Wang, T., Yang, J., Yang, H., Tang, L., Yang, D., 2025. Revealing the Long-Term Catchment-Scale Carbon Budget Dynamics on the Permafrost-Dominated Eastern Tibetan Plateau. Global Biogeochemical Cycles 39, e2025GB008743. https://doi.org/https://doi.org/10.1029/2025GB008743

Li, M., Peng, C., Zhang, K., Xu, L., Wang, J., Yang, Y., Li, P., Liu, Z., He, N., 2021. Headwater stream ecosystem: an important source of greenhouse gases to the atmosphere. Water Research 190, 116738. https://doi.org/10.1016/j.watres.2020.116738

Li, X., Wang, J., Lin, J., Yin, W., Shi, Y.Y., Wang, L., Xiao, H.B., Zhong, Z.M., Jiang, H., Shi,

677 Z.H., 2022. Hysteresis analysis reveals dissolved carbon concentration – discharge
678 relationships during and between storm events. Water Research 226, 119220.
679 https://doi.org/10.1016/j.watres.2022.119220
680 Li, Ziliang, Kang, L., Wang, L., Wanek, W., Zhang, D., Wang, G., Lambers, H., Peñuelas, J., Jiang,
681 M., Yang, Y., 2025. Accelerated soil phosphorus cycling upon abrupt permafrost thaw. Nat.
682 Clim. Chang. https://doi.org/10.1038/s41558-025-02445-4
683 Li, Z., Liu, F., Li, H., Liu, M., Li, Zongxing, Feng, Q., Xu, B., Liu, X., 2025. Driving forces of the
684 spatiotemporal supply pattern of runoff in the source region of Yellow River. Journal of
685 Hydrology: Regional Studies 60, 102515.
686 https://doi.org/https://doi.org/10.1016/j.ejrh.2025.102515
687 Liu, G., Li, S., Song, K., Wang, X., Wen, Z., Kutser, T., Jacinthe, P.-A., Shang, Y., Lyu, L., Fang,
688 C., Yang, Y., Yang, Q., Zhang, B., Cheng, S., Hou, J., 2021. Remote sensing of CDOM and
689 DOC in alpine lakes across the Qinghai-Tibet Plateau using Sentinel-2A imagery data.
690 Journal of Environmental Management 286, 112231.
691 https://doi.org/10.1016/j.jenvman.2021.112231
692 Liu, H., 2023. Human activity intensity dataset of the Qinghai-Tibet Plateau (2000-2020).
693 National Tibetan Plateau Data Center. https://doi.org/10.3974/geodb.2023.07.08.V1
694 Liu, L., Yang, S., Wang, S., Hu, J., Li, C., Yi, Y., 2025. Influence of the Cascade Reservoir
695 Operation of the Yellow River on the Hydrological Regime of the Main Stream of the Yellow
696 River. Yellow River 47, 42-47+77.
697 Liu, P., Zeng, H., Qi, L., Degen, A.A., Boone, R.B., Luo, B., Huang, M., Peng, Z., Qi, T., Wang,
698 W., 2024. Vegetation redistribution is predicted to intensify soil organic carbon loss under

699 future climate changes on the Tibetan Plateau. Science of The Total Environment 932,
700 173034.
701 Lv, Z., Ran, X., Liu, J., Feng, Y., Zhong, X., Jiao, N., 2024. Effectiveness of Chemical Oxygen
702 Demand as an Indicator of Organic Pollution in Aquatic Environments. Ocean-Land-Atmos
703 Res 3, 0050. https://doi.org/10.34133/olar.0050
704 Ma, M., Wang, Z., Zang, H., Wang, W., Wei, M., Cui, H., 2023. Runoff Simulation and Prediction
705 in the Source Region of the Yellow River Based on SSP Scenarios. Journal of North China
706 University of Water Resources and Electric Power (Natural Science Edition) 44, 31–40.
707 https://doi.org/10.19760/j.ncwu.zk.2023054
708 Ma, W., Wu, T., Wu, X., Yang, S., Li, R., Zhou, S., Li, X., Zhu, X., Hao, J., Ni, J., 2023. Carbon
709 budgets and environmental controls in alpine ecosystems on the Qinghai-Tibet Plateau.
710 Catena 229, 107224.
711 Maavara, T., Chen, Q., Van Meter, K., Brown, L.E., Zhang, J., Ni, J., Zarfl, C., 2020. River dam
712 impacts on biogeochemical cycling. Nature Reviews Earth & Environment 1, 103–116.
713 Maavara, T., Lauerwald, R., Regnier, P., Van Cappellen, P., 2017. Global perturbation of organic
714 carbon cycling by river damming. Nature communications 8, 15347.
715 Meng, Y., Duan, K., Shi, P., Shang, W., Li, S., Cheng, Y., Xing, L., Chen, R., He, J., 2023.
716 Sensitive temperature changes on the Tibetan Plateau in response to global warming.
717 Atmospheric Research 294, 106948.
718 Peng, S., 2025a. 1-km monthly precipitation dataset for China (1901-2024). National Tibetan
719 Plateau Data Center. https://doi.org/10.5281/zenodo.3114194
720 Peng, S., 2025b. 1-km monthly mean temperature dataset for China (1901-2024). National Tibetan

721 Plateau Data Center. https://doi.org/10.11888/Meteoro.tpdc.270961
722 Regnier, P., Resplandy, L., Najjar, R.G., Ciais, P., 2022. The land-to-ocean loops of the global
723 carbon cycle. Nature 603, 401–410. https://doi.org/10.1038/s41586-021-04339-9
724 San, M., Jia, S., Yang, C., Liu, J., Yu, Z., Fang, W., Shang, J., Ming, B., Guo, Y., Cheng, L., 2025.
725 Runoff Prediction in the Source Region of the Yellow River Basin Based on the CMIP6
726 Climate Model. Soil and Water Conservation in China 71-77+89.
727 https://doi.org/CNKI:SUN:ZGSB.0.2025-07-020
728 Shang, Y., Wen, Z., Liu, G., Fang, C., Yu, X., Liu, J., Song, K., 2026. Deciphering riverine
729 CODMn sources: driver identification and carbon cycle impacts. Ecological Indicators 190,
730 115312. https://doi.org/10.1016/j.ecolind.2026.115312
731 Vachon, D., Sponseller, R.A., Karlsson, J., 2021. Integrating carbon emission, accumulation and
732 transport in inland waters to understand their role in the global carbon cycle. Global Change
733 Biology 27, 719–727. https://doi.org/10.1111/gcb.15448
734 Wang, L., 2024. Difference and causes of runoff in different sections above Tangnaihai in the
735 source region of the Yellow River. Journal of Qinghai Normal University (Natural Science
736 Edition) 40, 99-104+112. https://doi.org/10.16229/j.cnki.issn1001-7542.2024313
737 Wang, M., Sun, K., Jia, J., Yu, G., Gao, Y., 2026. Unraveling the carbon fraction heterogeneity in
738 China’s Rivers: Hydrology, nutrients, and dam regulation. Water Research 288, 124591.
739 https://doi.org/https://doi.org/10.1016/j.watres.2025.124591
740 Wang, S., Benoit, G., Raymond, P.A., Yu, G., Zhou, F., Liu, S., Miao, C., Sun, K., Li, Z., Jia, J.,
741 2025. Dissolved carbon storage and flux dynamics in China’s inland waters over the past 30
742 years. National Science Review nwaf229.

743 Wang, S., Shen, M., Liu, W., Ma, Y., Shi, H., Zhang, J., Liu, D., 2022. Developing remote sensing
744 methods for monitoring water quality of alpine rivers on the Tibetan Plateau. GIScience &
745 Remote Sensing 59, 1384–1405. https://doi.org/10.1080/15481603.2022.2116078
746 Wang, T., Yang, D., Yang, Y., Piao, S., Li, X., Cheng, G., Fu, B., 2020. Permafrost thawing puts
747 the frozen carbon at risk over the Tibetan Plateau. Science Advances 6, eaaz3513.
748 https://doi.org/10.1126/sciadv.aaz3513
749 Wang, W., Zhong, J., Li, S.-L., Ulloa-Cedamanos, F., Xu, Sen, Chen, S., Lai, M., Xu, Sheng, 2023.
750 Constraining the sources and cycling of dissolved inorganic carbon in an alpine river, eastern
751 Qinghai-Tibet Plateau. Science of The Total Environment 901, 166262.
752 https://doi.org/10.1016/j.scitotenv.2023.166262
753 Wang, X., Wu, Y., Luo, M., Katsanou, K., Wenninger, J., Bol, R., 2025. Exports of organic matter,
754 phosphorus and nitrogen from Sichuan Basin: A critical region regulating water quality of the
755 Upper Yangtze River, China. Journal of Hydrology 662, 133889.
756 https://doi.org/https://doi.org/10.1016/j.jhydrol.2025.133889
757 Wen, W., Gao, L., Cheng, H., Xiao, L., Zhang, S., Li, S., Jiang, X., Xia, X., 2024. Legacy and
758 alternative perfluoroalkyl acids in the Yellow River on the Qinghai-Tibet Plateau: Levels,
759 spatiotemporal characteristics, and multimedia transport processes. Water Research 262,
760 122095. https://doi.org/10.1016/j.watres.2024.122095
761 Wu, Y., Su, H., Cheng, L., Qin, S., Zou, K., Liu, Y., Zhou, J., Liu, P., Zhang, L., 2024. Exploring
762 hydrological controls on dissolved organic carbon export dynamics in a typical flash flood
763 catchment using a process-based model. Science of The Total Environment 921, 171139.
764 https://doi.org/10.1016/j.scitotenv.2024.171139

765 Xu, S., Li, S.-L., Bufe, A., Klaus, M., Zhong, J., Wen, H., Chen, S., Li, L., 2024. Escalating
766 Carbon Export from High-Elevation Rivers in a Warming Climate. Environ. Sci. Technol. 58,
767 7032–7044. https://doi.org/10.1021/acs.est.3c06777
768 Yan, N., Qiu, Z., Zhang, C., Yan, Y., Liu, D., 2025. Landsat monitoring reveals the history of river
769 organic pollution across China during 1984–2023. Water Research 275, 123210.
770 https://doi.org/10.1016/j.watres.2025.123210
771 Yan, Y., Lauerwald, R., Wang, X., Regnier, P., Ciais, P., Ran, L., Gao, Y., Huang, L., Zhang, Y.,
772 Duan, Z., 2023. Increasing riverine export of dissolved organic carbon from China. Global
773 Change Biology 29, 5014–5032.
774 Yang, J., Wang, T., Yang, D., Yang, Y., 2023. Insights into runoff changes in the source region of
775 Yellow River under frozen ground degradation. Journal of Hydrology 617, 128892.
776 https://doi.org/10.1016/j.jhydrol.2022.128892
777 Yang, M., Li, S., Wang, S., Huang, Q., Shen, Q., Kang, Y., Shi, M., Zhang, Y., Luo, D., 2025.
778 Latitudinal gradient and environmental drivers of soil organic carbon in permafrost regions of
779 the Headwater Area of the Yellow River. Carbon Neutrality 4, 16.
780 Yao, T., Bolch, T., Chen, D., Gao, J., Immerzeel, W., Piao, S., Su, F., Thompson, L., Wada, Y.,
781 Wang, L., Wang, T., Wu, G., Xu, B., Yang, W., Zhang, G., Zhao, P., 2022. The imbalance of
782 the Asian water tower. Nat Rev Earth Environ 3, 618–632.
783 https://doi.org/10.1038/s43017-022-00299-4
784 Zeng, F., Song, C., Cao, Z., Xue, K., Lu, S., Chen, T., Liu, K., 2023. Monitoring inland water via
785 Sentinel satellite constellation: A review and perspective. ISPRS Journal of Photogrammetry
786 and Remote Sensing 204, 340–361. https://doi.org/10.1016/j.isprsjprs.2023.09.011

Zhang, Z., Zhang, L., Liu, Y., Jin, M., 2024. Responses of annual streamflow variability to annual precipitation, extreme climate events and large-scale climate phenomena in the Qinghai-Tibet Plateau. Journal of Hydrology 632, 130969. https://doi.org/10.1016/j.jhydrol.2024.130969

Zhao, W., Cheng, Y., Jian, J., Jiao, J., Cheng, C., Li, J., Chen, T., 2023. Water erosion changes on the Qinghai-Tibet Plateau and its response to climate variability and human activities during 1982–2015. CATENA 229, 107207. https://doi.org/10.1016/j.catena.2023.107207

Zhi, W., Appling, A.P., Golden, H.E., Podgorski, J., Li, L., 2024. Deep learning for water quality. Nat Water 2, 228–241. https://doi.org/10.1038/s44221-024-00202-z

Supplementary materials

Riverine organic matter dynamics in the headwater of the Yellow River under climate change

Xiaoxiao Wang [1,2], Jie Wang [1], Tianqing Ren [1], Jun Zhou [3]

[1] School of Geographical Sciences, China West Normal University, Nanchong 637009, China

[2] Sichuan Provincial Engineering Research Center of Monitoring and Control for Soil Erosion in Dry Valleys, China West Normal University, Nanchong 637009, China

[3] Institute of Mountain Hazards and Environment, Chinese Academy of Sciences, Chengdu 610213, China

Corresponding author

Xiaoxiao Wang

E-mail address: wxx1989@cwnu.edu.cn

School of Geographical Sciences, China West Normal University, Nanchong 637009, China

Text S1 Delta Change Method

Future climate data are often systematically biased, so the first step in using climate model data is often bias correction. This study uses delta correction for future climate following Cao et al. (2026). The delta method sums the difference between the past and present modelled climate and the present observed climate (Beyer et al., 2020). Thus, delta assumes that local (i.e., grid-cell-specific) model biases are constant over time(Maraun et al., 2017). For the temperature variable, the bias of the geographic location x is given by the difference between the current observed temperature and the modelled temperature, $T_{emp}(x,0) - T_{sim}^{raw}(x,0)$. The bias-corrected temperature at some time in the past x is estimated to be:

$$T_{sim}^{DM}(x,t) := T_{emp}(x,0) + \left(T_{sim}^{raw}(x,t) - T_{sim}^{raw}(x,0)\right) \quad (1)$$

$$= T_{sim}^{raw}(x,t) + \left(T_{emp}(x,0) - T_{sim}^{raw}(x,0)\right) \quad (2)$$

The second expression ($T_{sim}^{DM}(x,t)$) illustrates an alternative approach, where the local deviation of the day is added to the local simulated temperature at time t. The deviation of the day is given by the difference between the current observed temperature and the simulated temperature.

The lower limit of precipitation is zero, and the order of magnitude of precipitation varies from region to region. Therefore, multiplicative rather than additive bias corrections are more common when applying delta to precipitation, which is equivalent to applying modelled relative changes to observed data(Maraun et al., 2017). Similar to temperature, biased precipitation is estimated as:

$$P_{sim}^{DM}(x,t) := P_{obs}(x,0) * \frac{P_{sim}^{raw}(x,t)}{P_{sim}^{raw}(x,0)} \quad (3)$$

$$= P_{obs}(x,t) * \frac{P_{sim}^{raw}(x,t)}{P_{sim}^{raw}(x,0)} \quad (4)$$

We correct the future climate data for 2025-2100 using historical climate data for 2014-2024 and NEX-GDDP-CMIP6 data for the same period, and validate it with historical climate data for 2014-2024 and corrected NEX-GDDP-CMIP6 data. Future climate conditions were represented for the periods 2025-2040, 2041-2070, 2071-2100, respectively. To ensure result reliability, the results were simultaneously averaged using different nationally developed models.

Table S1 Definitions of riverine indicators sensitive to organic matter concentrations, following Yan et al. (2025).

Indicators	Equation
NDCI	$NDCI = (SR_{red} - SR_{green}) / (SR_{red} + SR_{green})$
OC_Index	$OC_Index = (SR_{red} + SR_{nir}) / (SR_{blue} + SR_{swir1})$
Hue Angel	$X = 11.053 \times SR_{ultrablue} + 6.950 \times SR_{blue} + 51.135 \times SR_{green} + 34.475 \times SR_{red}$ $Y = 1.320 \times SR_{ultrablue} + 21.053 \times SR_{blue} + 66.023 \times SR_{green} + 18.034 \times SR_{red}$ $Z = 58.083 \times SR_{ultrablue} + 34.931 \times SR_{blue} + 2.606 \times SR_{green} + 0.016 \times SR_{red}$ $x = X / (X + Y + Z)$ $y = Y / (X + Y + Z)$ $\alpha = [\arctan((y - 1/3) / (x - 1/3)) \bmod 2\pi] \times 180 / \pi$

Table S2 Test and validation scores of different models for COD_{Mn} prediction using satellite data.

No.	Model	Test score	Validation score
1	LightGBMLarge_BAG_L1	-0.22325	-0.66913
2	RandomForestMSE_BAG_L1	-0.2425	-0.661322
3	ExtraTreesMSE_BAG_L1	-0.24681	-0.672584
4	XGBoost_BAG_L1	-0.31248	-0.674913
5	CatBoost_BAG_L1	-0.34349	-0.649774
6	CatBoost_r177_BAG_L1	-0.34857	-0.652313
7	RandomForestMSE_BAG_L2	-0.36146	-0.636188
8	ExtraTreesMSE_BAG_L2	-0.36618	-0.621578
9	NeuralNetTorch_BAG_L2	-0.36816	-0.610234
10	WeightedEnsemble_L3	-0.37258	-0.602517
11	CatBoost_r177_BAG_L2	-0.38146	-0.625719
12	WeightedEnsemble_L2	-0.38381	-0.630267
13	CatBoost_BAG_L2	-0.38433	-0.623588
14	XGBoost_BAG_L2	-0.38697	-0.6598
15	LightGBM_r131_BAG_L1	-0.38935	-0.651746
16	NeuralNetFastAI_BAG_L2	-0.39335	-0.619413
17	LightGBMXT_BAG_L1	-0.39513	-0.673662
18	LightGBMXT_BAG_L2	-0.39965	-0.629565
19	LightGBMLarge_BAG_L2	-0.40136	-0.667139
20	LightGBM_BAG_L2	-0.42184	-0.637511
21	LightGBM_BAG_L1	-0.44421	-0.655706
22	NeuralNetTorch_BAG_L1	-0.51521	-0.722361
23	NeuralNetTorch_r79_BAG_L1	-0.6058	-0.68912
24	NeuralNetFastAI_BAG_L1	-0.68089	-0.773005

Table S3 Test and validation scores of different models for COD_{Mn} prediction based on geographical features.

No.	Model	Test score	Validation score	No.	Model	Test score	Validation score
1	LightGBMLarge_BAG_L1	-0.081138	-0.2644	**19**	CatBoost_r69_BAG_L1	-0.167949	-0.23341
2	XGBoost_r194_BAG_L1	-0.089043	-0.2592	**20**	LightGBM_r131_BAG_L1	-0.168802	-0.23719
3	ExtraTreesMSE_BAG_L1	-0.090097	-0.24898	**21**	LightGBM_BAG_L1	-0.176396	-0.26183
4	ExtraTrees_r42_BAG_L1	-0.092587	-0.25519	**22**	WeightedEnsemble_L2	-0.177354	-0.20715
5	RandomForest_r195_BAG_L1	-0.0953	-0.25655	**23**	NeuralNetTorch_r86_BAG_L1	-0.193151	-0.22308
6	XGBoost_r33_BAG_L1	-0.097439	-0.25877	**24**	NeuralNetTorch_r79_BAG_L1	-0.201559	-0.22065
7	RandomForestMSE_BAG_L1	-0.100664	-0.2697	**25**	NeuralNetTorch_BAG_L1	-0.20326	-0.25054
8	XGBoost_r89_BAG_L1	-0.112642	-0.2575	**26**	NeuralNetTorch_r14_BAG_L1	-0.204362	-0.2446
9	CatBoost_r9_BAG_L1	-0.116537	-0.24187	**27**	NeuralNetTorch_r30_BAG_L1	-0.212912	-0.2288
10	XGBoost_BAG_L1	-0.117449	-0.26967	**28**	NeuralNetFastAI_BAG_L1	-0.213711	-0.26241
11	CatBoost_r13_BAG_L1	-0.13718	-0.23871	**29**	NeuralNetFastAI_r191_BAG_L1	-0.214983	-0.2659
12	LightGBM_r188_BAG_L1	-0.148257	-0.24493	**30**	ExtraTrees_r172_BAG_L1	-0.217508	-0.26801
13	CatBoost_r177_BAG_L1	-0.153872	-0.23387	**31**	NeuralNetFastAI_r103_BAG_L1	-0.224872	-0.23766
14	CatBoost_r50_BAG_L1	-0.156083	-0.23575	**32**	NeuralNetFastAI_r102_BAG_L1	-0.229039	-0.26453
15	CatBoost_BAG_L1	-0.156563	-0.23661	**33**	NeuralNetTorch_r22_BAG_L1	-0.23428	-0.26398
16	LightGBMXT_BAG_L1	-0.15731	-0.24073	**34**	NeuralNetFastAI_r145_BAG_L1	-0.235515	-0.27573
17	LightGBM_r161_BAG_L1	-0.15873	-0.2379	**35**	NeuralNetFastAI_r11_BAG_L1	-0.374389	-0.45661
18	CatBoost_r137_BAG_L1	-0.160723	-0.23589	**36**	LightGBM_r96_BAG_L1	-0.428637	-0.47816

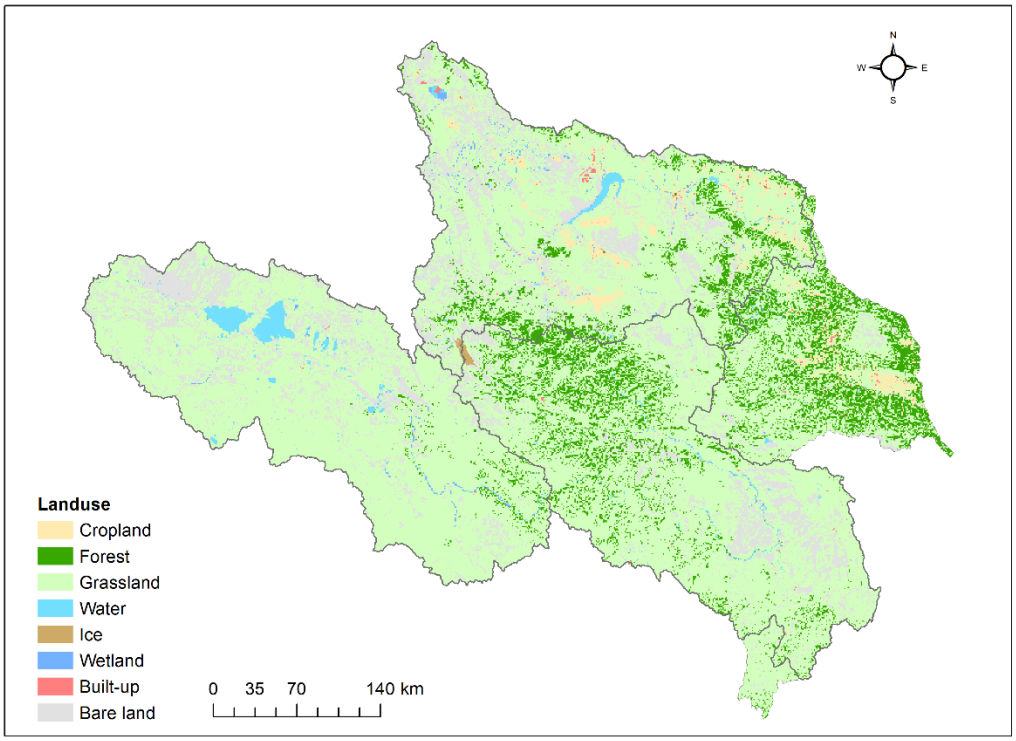


Fig.S1 Land use distribution across the three sub-basins (B1–B3) within the Yellow River source region.

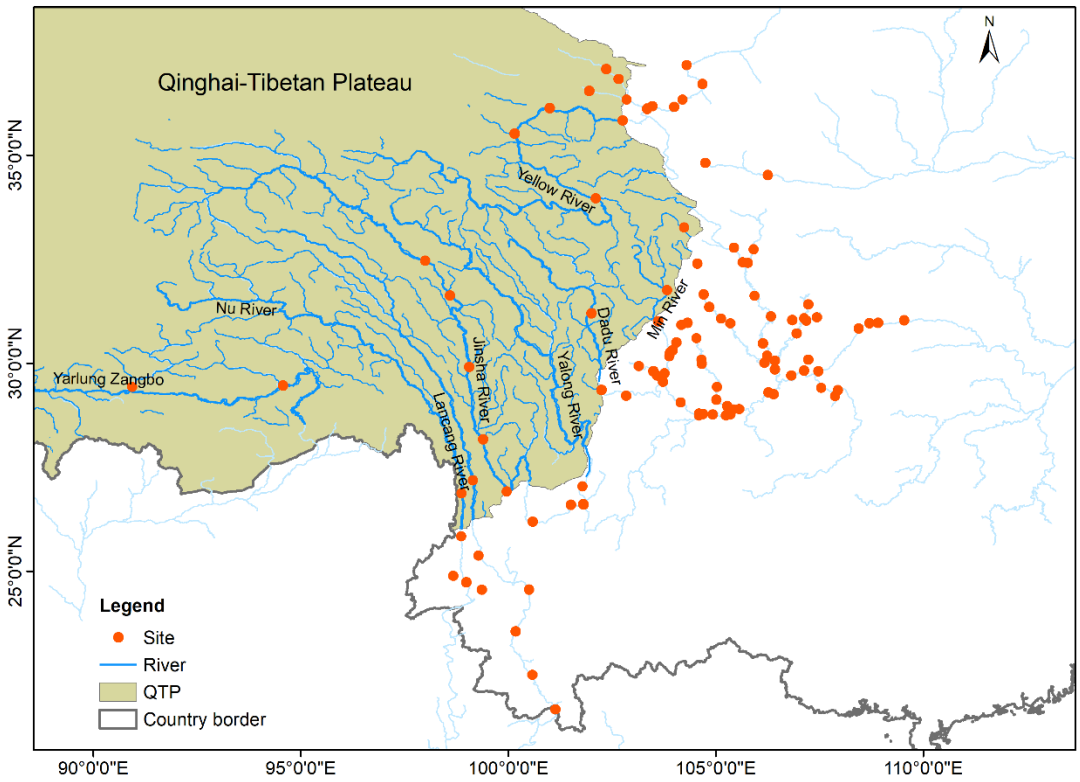


Fig.S2 Locations of data collection sites for model training across the Qinghai–Tibetan Plateau and adjacent areas.

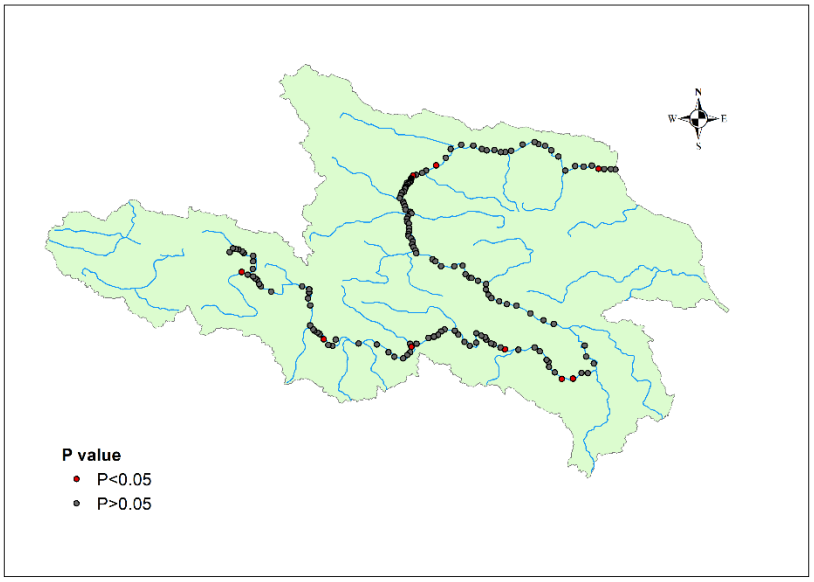


Fig.S3 Statistical significance of historical COD_{Mn} trends during 2014–2024. *P* values were obtained from the Mann–Kendall test.

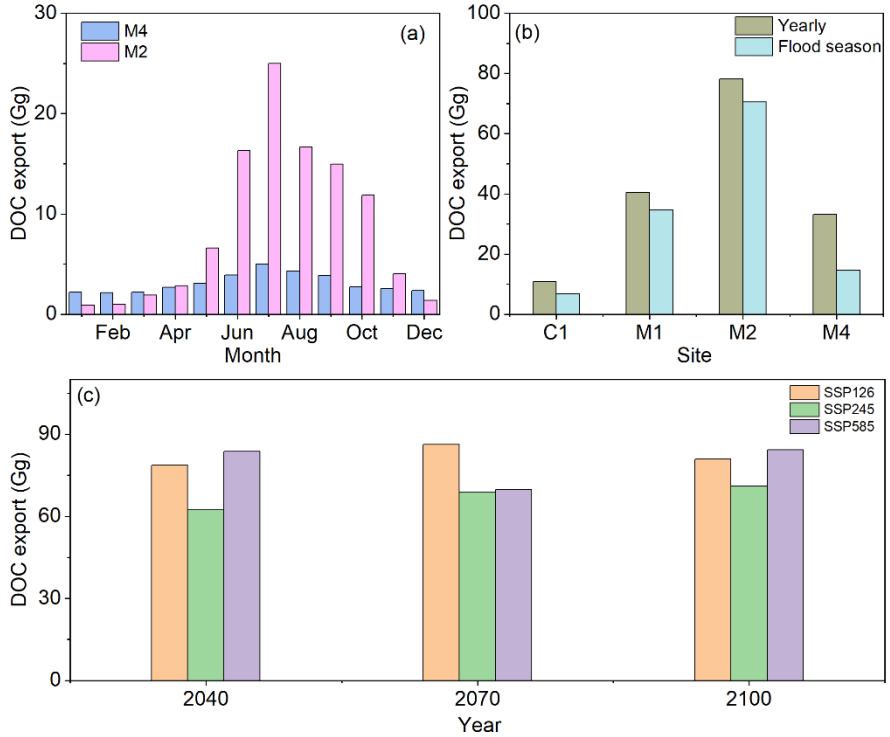


Fig.S4 Monthly average DOC export at sites M2 and M4 during 2014-2024 (a); comparison between annual and flood-season DOC exports (b); projected DOC export at M2 for 2040, 2070, and 2100 under SSP126, SSP245, and SSP585 scenarios (c).

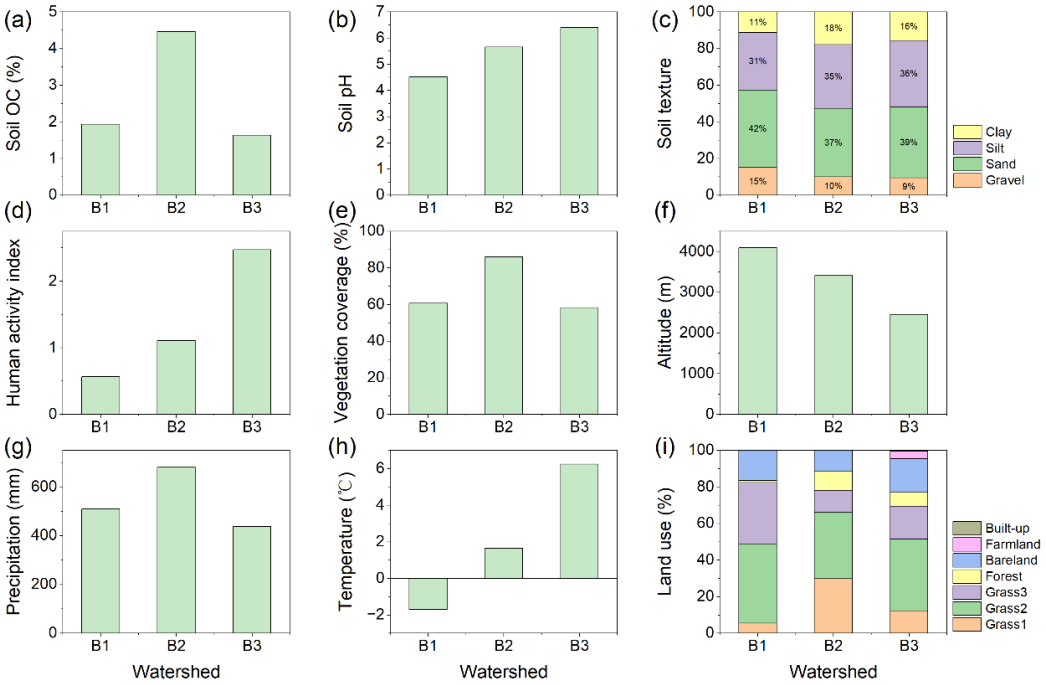


Fig.S5 Geographical characteristics of the sub-basins in the Yellow River source region. (a–c) Soil organic matter, pH, and texture; (d–f) human activity index, vegetation coverage, and altitude; (g–i) average precipitation and temperature over the last ten years, and land use in 2015.

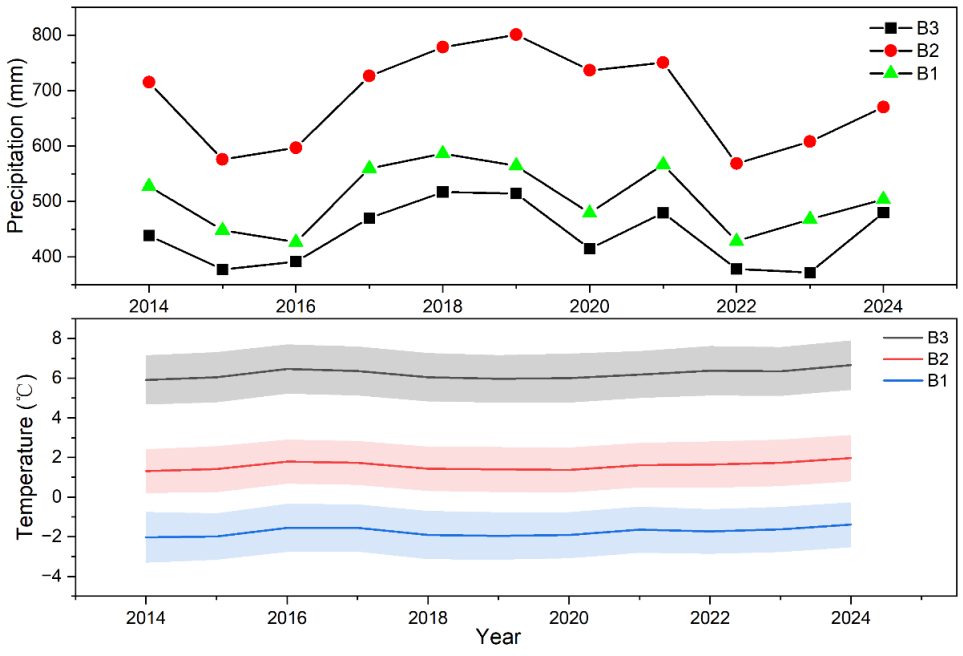


Fig.S6 Variations in precipitation and temperature averaged across different sub-basins of the Yellow River source region during 2014–2024.

References

Beyer, R., Krapp, M. and Manica, A. 2020. An empirical evaluation of bias correction methods for palaeoclimate simulations. Climate of the Past 16(4), 1493-1508.

Cao, Y., Yao, H., Zhang, C., Gu, C., Yang, L., Hao, R., Li, X., Wang, Z., Xiao, H., Wang, J., Shi, Z., 2026. Data-driven assessment of nitrogen and phosphorus buffering capacity across 460 Chinese watersheds: Spatial patterns, drivers, and future projections. Water Research 293, 125424.

Maraun, D., Shepherd, T.G., Widmann, M., Zappa, G., Walton, D., Gutiérrez, J.M., Hagemann, S., Richter, I., Soares, P.M. and Hall, A. 2017. Towards process-informed bias correction of climate change simulations. Nature Climate Change 7(11), 764-773